Spring 5-31-2013

Mathematical models for bistable nematic liquid crystal displays

Chenjing Cai
New Jersey Institute of Technology

ABSTRACT

MATHEMATICAL MODELS FOR BISTABLE NEMATIC LIQUID CRYSTAL DISPLAYS

by
Chenjing Cai

Bistable Liquid Crystal Displays (LCDs) offer the potential for considerable power savings, compared with conventional (monostable) LCDs. The existence of two (or more) stable field-free states that are optically-distinct means that contrast can be maintained in a display without an externally-applied electric field. An applied field is required only to switch the device from one state to the other, as needed. This dissertation focuses on theoretical models of a possible bistable nematic device, whose operating principle relies on controlling surface anchoring conditions. Switching between the two stable steady states is achieved by application of a transient electric field. A 1D model is considered first, and means are explored, by which the design may be optimized, in terms of optical contrast, manufacturing considerations, switching field strength and switching times. The compromises inherent in these conflicting design criteria are discussed. Motivated by a desire to improve on the results of this 1D model, and to test its robustness, a two-dimensional geometry is considered next, in which variable surface anchoring conditions are used to control the steady-state solutions and it is explored how different anchoring conditions can influence the number and type of solutions, and whether or not switching is possible between the states. A wide range of possible behaviors are found, including bistability, tristability and tetrastability, and it is investigated how the solution landscape changes as the boundary conditions are tuned. All of these investigations are based (for simplicity) on an assumption of uniform electric field within the nematic liquid crystal. To check the validity of this assumption, the study is concluded by formulating the problem with non-uniform field, and comparing the results to the uniform field case.

MATHEMATICAL MODELS FOR BISTABLE NEMATIC LIQUID CRYSTAL DISPLAYS

by
Chenjing Cai

A Dissertation
Submitted to the Faculty of
New Jersey Institute of Technology
Rutgers, The State University of Jersey - Newark
in Partial Fulfillment of the Requirements for the Degree of
Doctor of Philosophy in Mathematical Sciences

Department of Mathematical Sciences, NJIT
Department of Mathematics and Computer Sciences, Rutgers-Newark

May 2013

APPROVAL PAGE

MATHEMATICAL MODELS FOR BISTABLE NEMATIC LIQUID CRYSTAL DISPLAYS

Chenjing Cai

Dr. Linda J. Cummings, Co-Dissertation Advisor, Committee Member — Date
Associate Professor of Mathematical Sciences, NJIT

Dr. Lou Kondic, Co-Dissertation Advisor, Committee Member — Date
Professor of Mathematical Sciences, NJIT

Dr. Michael R. Booty, Committee Member — Date
Professor of Mathematical Sciences, NJIT

Dr. Peter Palffy-Muhoray, Committee Member — Date
Professor of Chemical Physics, Kent State University

Dr. Shahriar Afkhami, Committee Member — Date
Assistant Professor of Mathematical Sciences, NJIT

BIOGRAPHICAL SKETCH

Author: Chenjing Cai

Degree: Doctor of Philosophy

Date: May 2013

Undergraduate and Graduate Education:

- Doctor of Philosophy in Mathematical Sciences,
  New Jersey Institute of Technology, Newark, NJ, 2013
- Bachelor of Science in Applied Mathematics,
  Nanjing University, Nanjing, China, 2007

Major: Applied Mathematics

Presentations and Publications:

Cummings, L. J., Cai, C., Kondic, L., "Bifurcation properties of nematic liquid crystals exposed to an electric field: switchability, bistability and multistability," *Phys. Rev. E*, Submitted, 2013.

Cummings, L. J., Cai, C., Kondic, L., "Towards an optimal model for a bistable liquid crystal display device," *J. Eng. Math.* **80** (1), 21-38, 2013.

My dissertation is dedicated to my family. A special feeling of gratitude to my loving parents, Genyuan Cai and Suyun Chen whose words of encouragement and push for tenacity ring in my ears. I also dedicate this dissertation to my grandparents, Baowang Chen and Qiaoying Luo for their love, endless support and encouragement. My brother, Michael Cai has never left my side and are very special.

I dedicate this work and give special thanks to my wife, Jessie and my wonderful daughter, Alaina for being there for me throughout the entire doctorate program. Both of you have been my best cheerleaders.

ACKNOWLEDGMENT

I gratefully acknowledge the great help from my advisors, Linda J. Cummings and Lou Kondic. I would like to acknowledge informative and useful discussions with committee members P. Palffy-Muhoray, Shahriar Afkhami and Michael R. Booty. This work was supported by the NSF under grants DMS-0908158 and DMS-1211713. I also acknowledge partial support from King Abdullah University of Science and Technology (KAUST), funded by Award no. KUK-C1-013-04. I also gratefully acknowledge the help from fellow graduate, Xing Zhong.

TABLE OF CONTENTS

TABLE OF CONTENTS
(Continued)

Chapter **Page**

LIST OF TABLES

Table **Page**

LIST OF FIGURES

LIST OF FIGURES
(Continued)

Figure **Page**

LIST OF FIGURES
(Continued)

Figure **Page**

LIST OF FIGURES
(Continued)

Figure **Page**

LIST OF FIGURES
(Continued)

Figure **Page**

CHAPTER 1

INTRODUCTION

With the current sustained demand for portable interactive electronic devices with displays (phones, e-readers, netbooks, music players, etc.), there is considerable interest in methods by which their power consumption may be reduced. Lower power consumption gives improved battery lifetimes, and also allows smaller batteries to be used, offering increased portability. In many small electronic devices, the screen is responsible for a sizeable portion of the power consumption, therefore research into low-power electronic displays is potentially very lucrative. Most modern e-readers use "e-ink" (or closely-related) technology [18], which uses very little power; but most portable phones, netbooks and music players use conventional Liquid Crystal Display (LCD) technology in their displays, which has higher power consumption, but better optical properties.

E-ink technology utilizes a suspension of tiny spherical microcapsules dispersed in a clear carrier fluid. Each microcapsule contains positively charged white particles and negatively charged black ones. In a DC electric field, all white particles will move to one side of the microcapsules while the black ones move to the opposite side. If the electric field direction is reversed, so is the motion of white and black particles in the microcapsule. Hence, display contrast can be controlled by applying fields of appropriate polarities in different portions of the screen (individual pixels). Moreover, once the field is removed, the particles stay where they are within the microcapsule, so that a field is required only to change the state of the display. This is an example of simple bistable technology, since the microcapsules remain *stable* in a given state until an electric field is applied to change the state; and there are *two* such stable states.

Conventional LCD technology, on the other hand, requires continuous application of an electric field. At the simplest level, a thin layer of nematic liquid crystal (NLC) is sandwiched between two plates, and placed between crossed polarizers. The NLC is birefringent: depending on its molecular orientation, it can rotate the plane of polarized light. The molecular orientation within the NLC can be controlled by application of an electric field across the layer (its molecules, which are like little rods, align in an applied field). Typically, with the molecules aligned, the polarized light passing through the first polarizer is not rotated as it passes through the NLC layer. Thus, it cannot pass through the second, crossed, polarizer. With no applied field, however, the molecular orientation within the layer is different (dictated solely by boundary effects now, rather than the electric field); the polarized light is rotated as it passes through the NLC layer, and can pass through the second crossed polarizer. These two states are therefore optically-distinct when light is passed through (the first will be dark, the second bright), and form the basis of an electronic display. However, the electric field must be "on" to maintain the contrast between neighboring pixels, meaning that such displays are energetically expensive.

One way to reduce the power consumption of an LCD device is to design it so that there are two stable states for the molecular orientation in the absence of an applied electric field. Provided these stable states are optically-distinct, and may be switched from one to the other by transient application of an electric field, power consumption could rival that of e-ink technology, yet with superior optical properties.

Previous theoretical demonstrations of such (switchable) bistable devices have either relied on having bistable bounding surfaces, that is, surfaces at which there are two preferred director orientations at the surface [11, 15]; on having special (nonplanar) surface morphology within the cell that allows for two stable states (the Zenithal Bistable nematic Device (ZBD) [3] and the Post-Aligned Bistable nematic

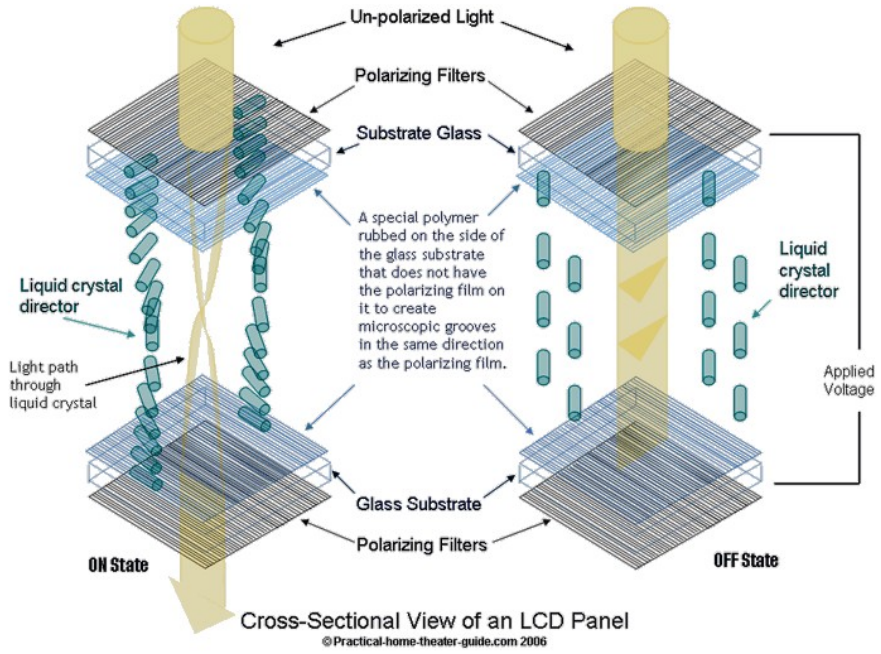

Figure 1.1 Schematic of a single cell, or pixel, in a conventional LCD device.

Source: http://www.practical-home-theater-guide.com/lcd-display.html.

Device (PABD) [29]; or, in the case of the Nemoptic BiNem technology [13], on flow effects and a very carefully applied electric field to effect the switching.

In this dissertation, we consider possible theoretical designs for such a bistable nematic LCD device. The proposed models, which have yet to be verified experimentally, build on earlier work by Cummings & Richardson [8], and rely on the premise that the bounding surfaces can be engineered so as to control the preferred molecular orientation of the nematic molecules. This is known as anchoring. The anchoring pretilt angle may be controlled by a variety of surface treatments; for example, mechanical or chemical treatments, nano-patterning, and surface irradiation, have all been shown to produce certain desired anchoring angles [5,7,14,16,19,24–26,28,30,32] with a high degree of control. The strength of the anchoring may also be controlled to some extent [17,21,25,26] by similar methods. As evidenced by these cited works, advances in the degree of control attainable are continually being made and, while not

quite yet a reality, "bespoke surfaces" with desired anchoring properties are becoming a real possibility for the near future.

In [8], only a limited subset of possible anchoring conditions was considered; bistability (with two-way switching) was found to be possible, but only under rather restrictive conditions (discussed below), which would make the device challenging to build successfully. Here we broaden our design parameters in order to alleviate these restrictions, and we further address the issue of which, among the family of possible designs, is the "best", according to certain metrics that we devise. These improvements of the original design should bring it much closer to physical realization.

It is also assumed, for most of the dissertation (Chapters 2 & 3), that the electric field utilized to switch the display is uniform. In reality, there is interaction between the electric field and the NLC, so that even if the electric field is uniform outside the layer, it will vary across the layer. A more careful treatment would take this into account; we address this issue in Chapter 4. Anticipating such variation to be insignificant in industrially-relevant regimes, we expect the uniform field assumption to be sufficient for the proof-of-principle investigation here.

The dissertation is laid out as follows: in Chapter 2, we investigate the simplest possible 1D model. In §2.1, we introduce the key dependent variables and the basic mathematical model. We first consider the steady-state model, before generalizing to the time-dependent case. §2.2 addresses the bistability at zero field, outlines our criteria for deciding whether one device is better than another, and derives the "benefit function" based on these criteria. §2.3 describes briefly the simulated annealing numerical approach taken to optimize this benefit function, and carries out the optimization in several stages, and then in §2.4, we draw our conclusions of the 1D case. In Chapter 3, we broaden the design further still, by allowing properties to vary in the plane of the device (a 2D model). §3.1 motivates this extension; §3.2 introduces the extended mathematical model; §3.3 outlines the numerical approach

taken, and §3.5 summarizes and discusses our key findings. In Chapter 4, we consider the model with non-uniform electric field. Finally we briefly discuss possible future extensions of our work in Chapter 5.

The work of Chapter 2 has been accepted for publication in the Journal of Engineering Mathematics [9], and the work of Chapter 3 is under consideration for publication in Physical Review E [10].

CHAPTER 2

1D MODEL OF A BISTABLE DISPLAY DEVICE

We begin by investigating the properties of the simplest possible device: a thin layer of nematic liquid crystal (NLC) sandwiched between two flat parallel bounding plates, across which a uniform electric field may be applied. This is an idealization of a single pixel within a bistable Liquid Crystal Display (LCD), intended to provide a "proof of principle" that bistability in such a setup may be achievable under the right conditions. Part of our aim in this chapter is to determine what these conditions are.

2.1 Mathematical Modeling: Basic Device Design

The basic setup is a layer of nematic liquid crystal (NLC), sandwiched between parallel bounding surfaces at $z^* = 0$ and $z^* = h^*$. Star superscripts will be used throughout to denote dimensional quantities, and will be dropped when we nondimensionalize. The molecules of the NLC are rod-like, which imparts anisotropy. The molecules like to align locally, which may be modeled by associating an elastic energy with any deviations from uniform alignment (§2.1.1 below). The local average molecular orientation is described by a director field $\boldsymbol{n}$, a unit vector, and in our simple model we assume that this director field is constrained to lie in a plane, the (x^*, z^*)-plane. The directions $+\boldsymbol{n}$ and $-\boldsymbol{n}$ are considered indistinguishable within the standard theory. We assume further that properties do not vary in the x^* direction, thus the director field may be expressed in terms of a single angle $\theta(z^*, t^*)$,

$$\boldsymbol{n} = (\sin\theta, 0, \cos\theta), \tag{2.1}$$

and that the electric field throughout the NLC layer is uniform: $\boldsymbol{E}^* = E^*(0, 0, 1)$. The anchoring pretilt angle is denoted by α in our model, with subscripts used to

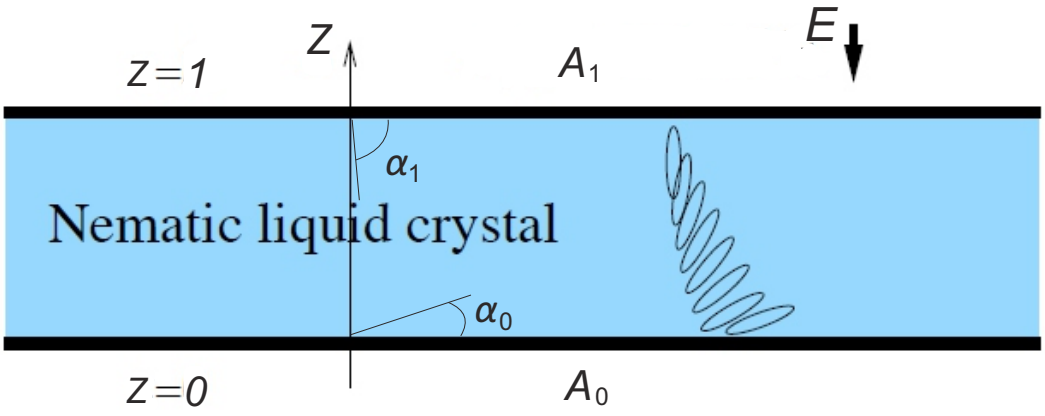

Figure 2.1 Sketch showing the setup and summarizing the key parameters in the dimensionless coordinates.

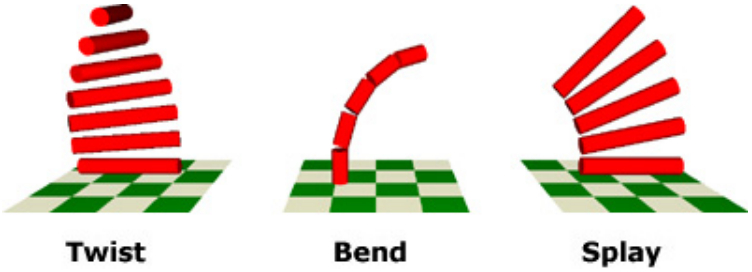

Figure 2.2 Sketch showing the three basic elastic contributions, corresponding to the three basic elastic deformations from which all others may be composed.

Source: http://lcp.elis.ugent.be/tutorials/lc/lc2.

distinguish the preferred value of θ at either interface (see Figure 2.1). We shall assume that surface anchoring angles α and strengths A^* are adjustable parameters in the modeling, within a range of physically-realistic values.

We begin by considering the equations and boundary conditions when time-dependence is neglected (this would be appropriate if, for example, the applied field was varied only slowly).

2.1.1 Steady-state Energetics

The free energy of the liquid crystal layer, in the presence of an applied electric field and with specified anchoring conditions at each bounding surface, has several contributions. The bulk free energy density consists of elastic, dielectric and flexoelectric contributions W_e^*, W_d^*, W_f^*, see, e.g. DeGennes & Prost [12]. The elastic energy W_e^* has three contributions, corresponding to the three basic elastic deformations (see Figure 2.2 equation (2.2) below) from which all others may be composed. The dielectric contribution to the energy density, W_d^*, causes molecules to align in an applied field, normally with their long axis parallel to the applied field direction. It depends only on the magnitude of the applied field so the distortion produced is the same whether the applied field is $\boldsymbol{E}^*$ or -$\boldsymbol{E}^*$. The flexoelectric contribution to the energy density, W_f^*, arises because the NLC molecules are asymmetric, and contain a small permanent electric dipole. This can interact with an applied electric field to produce orientational distortion (splay and bend, see Figure 2.3) within the NLC, so the distortion produced is different if the electric field is reversed.

In our model with the uniform field assumption, these effects are given by

$$2W_e^* = K_1^*(\nabla^* \cdot \boldsymbol{n})^2 + K_2^*(\boldsymbol{n} \cdot \nabla^* \times \boldsymbol{n})^2 + K_3^*((\nabla^* \times \boldsymbol{n}) \times \boldsymbol{n})^2, \tag{2.2}$$

$$2W_d^* = -\varepsilon_0^*(\varepsilon_\parallel - \varepsilon_\perp)(\boldsymbol{n} \cdot \boldsymbol{E}^*)^2, \tag{2.3}$$

$$W_f^* = -\boldsymbol{E}^* \cdot (e_1^*(\nabla^* \cdot \boldsymbol{n})\boldsymbol{n} + e_3^*(\nabla^* \times \boldsymbol{n}) \times \boldsymbol{n}), \tag{2.4}$$

where K_1^*, K_2^* and K_3^* are elastic constants, ε_0^* is the permittivity of free space, $\varepsilon_\parallel$ and $\varepsilon_\perp$ are the relative dielectric permittivities parallel and perpendicular to the long axis of the nematic molecules, and e_1^* and e_3^* are flexoelectric constants [4, 12, 27]. When the dielectric anisotropy, $\varepsilon_\parallel - \varepsilon_\perp > 0$, W_d^* is decreased by the director field $\boldsymbol{n}$ aligning with the field, thus molecules will align with their long axis parallel to an applied field in this case (if the dielectric anisotropy is negative, molecules will align perpendicular to an applied field). We assume positive dielectric anisotropy

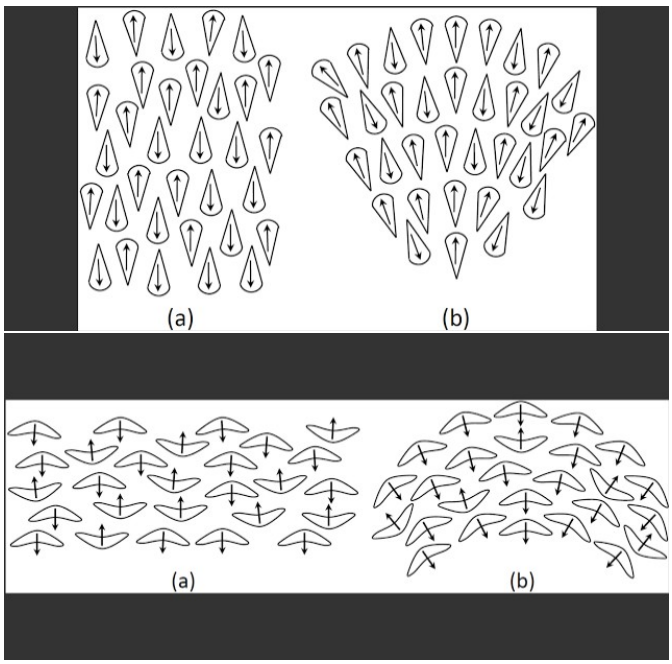

Figure 2.3 Sketch showing the orientational distortion (splay and bend) within the NLC, produced by the flexoelectric effect interacting with an applied electric field.

Source: http://brindabankundu.blogspot.com/2011/06/flexoelectricity.html.

throughout. The terms in K_1^*, K_2^* and K_3^* represent 'splay', 'twist' and 'bend' of the director field, respectively (see Figure 2.2). With the director field $\boldsymbol{n}$ as given by (2.1), with $\theta = \theta(z^*)$, the electric field $\boldsymbol{E^*} = E^*(0, 0, 1)$, and the common simplifying assumption $K_1^* = K_3^* = K^*$, the total bulk free energy density $W^* = W_e^* + W_d^* + W_f^*$ simplifies. Introducing the nondimensional forms $W = K^* W^*/h^{*2}$ and $z = z^*/h^*$,

$$W = \frac{\theta_z^2}{2} - \mathcal{D}\cos^2\theta + \frac{\mathcal{F}\theta_z}{2}\sin 2\theta, \tag{2.5}$$

where

$$\mathcal{D} = \frac{h^{*2}E^{*2}\varepsilon_0^*(\varepsilon_\parallel - \varepsilon_\perp)}{2K^*}, \quad \mathcal{F} = \frac{h^*E^*(e_1^* + e_3^*)}{K^*} \tag{2.6}$$

are dimensionless constants. With representative characteristic values

$$h^* \sim 1\mu\text{m},\ E^* \sim 1\text{V}\mu\text{m}^{-1},\ e_1^* + e_3^* \sim 5 \times 10^{-11}\text{C m}^{-1},\ K^* \sim 1 \times 10^{-11}\text{N},$$

$$\varepsilon_{\parallel} - \varepsilon_{\perp} \sim 5,$$

[2,11,22] both $\mathcal{D}$ and $\mathcal{F}$ are $O(1)$. We emphasize that the values given above are *not* intended to be absolute in what follows; a fair degree of variation about these values is possible, and indeed, many different combinations of dimensional parameter values will lead to the same model in dimensionless form. Note also that these parameters $\mathcal{D}$ and $\mathcal{F}$ are not independent; the ratio

$$\Upsilon = \frac{\mathcal{F}^2}{\mathcal{D}} = \frac{2(e_1^* + e_3^*)^2}{K^* \varepsilon_0^* (\varepsilon_{\parallel} - \varepsilon_{\perp})} \tag{2.7}$$

is a material parameter, independent of device design, so must remain fixed. We consider the case in which the dielectric anisotropy $\varepsilon_{\parallel} - \varepsilon_{\perp} > 0$, so that $\mathcal{D} > 0$ always (this means that an applied field acts to align molecules with the field, rather than perpendicular to it). The parameter $\mathcal{F}$, characterizing the dimensionless strength of the applied electric field, will, however, change sign if the electric field direction is reversed. Since the representative parameter values listed above give $\Upsilon \approx 10$, we assign this value to Υ throughout our computations, again noting that this single value corresponds to many different possible combinations of dimensional parameters: $\Upsilon = 10$ henceforth.

The surface energy density models the preferred behavior of the molecules at each bounding surface. We use the formula proposed by Rapini & Papoular [23]; if $g^*_{\{0,h^*\}} = (K^*/h^*) g_{\{0,1\}}$ are the surface energies per unit length at the boundaries $z^* = 0$, h^*, then

$$g_{0,1} = \frac{\mathcal{A}_{\{0,1\}}}{2} \sin^2(\theta - \alpha_{\{0,1\}}), \quad \text{where} \quad \mathcal{A}_{\{0,1\}} = \frac{h^* A^*_{\{0,h^*\}}}{K^*}. \tag{2.8}$$

Here $A^*_{\{0,h^*\}}$ are the anchoring strengths at $z^* = 0$, h^* and $\alpha_{\{0,1\}}$ are the preferred angles; as $A^* \to \infty$ the anchoring becomes strong, and the director angle is forced to take the value α. The sketch in Figure 2.1 summarizes the setup and notation.

The total (dimensionless) free energy for the system is given by

$$J = \int_0^1 W(\theta, \theta_z)\, dz + g_0(\theta)|_{z=0} + g_1(\theta)|_{z=1}\,,$$

and equilibrium solutions to the system are those functions $\theta(z)$ that minimize J. The standard calculus of variations approach, with $\theta(z) \mapsto \theta(z) + \epsilon\eta(z)$ $(0 < \epsilon \ll 1)$ leads to $J \mapsto J[\theta + \epsilon\eta] = J_0 + \epsilon J_1 + \epsilon^2 J_2 + O(\epsilon^3)$, and for $\theta(z)$ to be a minimizer of J we require $J_1 = 0$, $J_2 > 0$, for all admissible variations η (the condition on J_2 ensures we have a minimum, rather than a maximum, of the free energy). After Taylor expansion, the expression for J_1 is found to be

$$J_1 = \int_0^1 (\eta W_\theta + \eta_z W_{\theta_z})\, dz + \eta g_{1\theta}|_{z=1} + \eta g_{0\theta}|_{z=0}\,.$$

A further integration by parts leads to

$$J_1 = \int_0^1 \eta \left(W_\theta - \left(W_{\theta_z}\right)_z\right) dz + \eta(g_{1\theta} + W_{\theta_z})|_{z=1} + \eta(g_{0\theta} - W_{\theta_z})|_{z=0}\,;$$

the condition that this vanish for all admissible variations $\eta(z)$ leads to the usual Euler-Lagrange equation for θ, subject to boundary conditions on $z = 0$, 1:

$$W_\theta - \left(W_{\theta_z}\right)_z = 0, \qquad (g_{0\theta} - W_{\theta_z})|_{z=0} = 0, \qquad (g_{1\theta} + W_{\theta_z})|_{z=1} = 0. \tag{2.9}$$

We note that the second variation J_2 is easily calculated to be

$$2J_2 = \int_0^1 \{\eta^2[W_{\theta\theta} - (W_{\theta\theta_z})_z] + \eta_z^2 W_{\theta_z\theta_z}\} dz + \eta^2(g_{1\theta\theta} + W_{\theta\theta_z})\big|_{z=1} + \eta^2(g_{1\theta\theta} - W_{\theta\theta_z})\big|_{z=0} \tag{2.10}$$

so that the stability of any steady solutions calculated may be checked.

2.1.2 Time-dependent Energetics: Gradient Flow

The weak (integral) form of the above steady-state minimization may be written

$$\langle W_\theta, \eta \rangle + \langle W_{\theta_z}, \eta_z \rangle + g_{1\theta}\eta|_{z=1} + g_{0\theta}\eta|_{z=0} = 0,$$

where $\langle A, B \rangle = \int_0^1 AB dz$. In reality of course, if the system is not at equilibrium then it will evolve over time towards a steady state described by the above equations. A truly accurate description of this dynamic process requires the full equations of nematodynamics [12, 20], which couple flow to director reorientation. For our explorations of multidimensional parameter space that follow, however, this model is extremely computationally intensive and instead we follow several other authors (e.g. Kedney & Leslie [15] and Davidson & Mottram [11]) in assuming that the system evolves in the direction that minimizes its total free energy (a gradient flow). Both bulk and surface components will evolve in this way, and this process may be represented as

$$\langle \tilde{\mu}\theta_t, \eta \rangle + \langle W_\theta, \eta \rangle + \langle W_{\theta_z}, \eta_z \rangle + [\tilde{\nu}\theta_t\eta + g_{1\theta}\eta]|_{z=1} + [\tilde{\nu}\theta_t\eta + g_{0\theta}\eta]|_{z=0} = 0,$$

where $\tilde{\mu}$ and $\tilde{\nu}$ may be interpreted as dimensionless bulk and surface rotational viscosities, respectively. With the natural choice of dimensionless time set by

$$t = t^* \frac{K^*}{\tilde{\mu}^* h^{*2}} \tag{2.11}$$

(where $\tilde{\mu}^*$ is the dimensional rotational viscosity of the NLC molecules, typically around 0.1 N s m^{-2}), $\tilde{\mu} = 1$. The integration by parts carried out above then leads to the evolution equation and boundary conditions

$$\theta_t + W_\theta - \left(W_{\theta_z}\right)_z = 0,$$

$$(\tilde{\nu}\theta_t + g_{0\theta} - W_{\theta_z})|_{z=0} = 0, \qquad (\tilde{\nu}\theta_t + g_{1\theta} + W_{\theta_z})|_{z=1} = 0.$$

With bulk and surface energy densities given by (2.5), (2.8), this system becomes

$$\theta_t = \theta_{zz} - \mathcal{D}\sin 2\theta, \tag{2.12}$$

$$\tilde{\nu}\theta_t = \theta_z - \frac{\mathcal{A}_0}{2}\sin 2(\theta - \alpha_0) + \frac{\mathcal{F}}{2}\sin 2\theta \quad \text{on } z = 0, \tag{2.13}$$

$$-\tilde{\nu}\theta_t = \theta_z + \frac{\mathcal{A}_1}{2}\sin 2(\theta - \alpha_1) + \frac{\mathcal{F}}{2}\sin 2\theta \quad \text{on } z = 1, \tag{2.14}$$

with $\mathcal{D}$ (dimensionless dielectric coefficient), $\mathcal{F}$ (dimensionless field strength) and $\mathcal{A}_{\{0,1\}}$ (dimensionless surface energy) given by (2.6) and (2.8). This model is closed by specification of an initial condition $\theta(z, 0)$. When θ is independent of time, this is exactly the steady-state model (2.9).

Our strategy is to solve the steady-state model at zero field to find the two solutions of lowest energy, then use our time-dependent model (2.12)–(2.14) to investigate the conditions under which switching between the two stable steady states is possible, by application of a transient electric field. Until we take switching time into account as part of our device optimization (§2.3.4), the time of application of the field is fixed at $t = 25$ in our simulations; with the time scaling chosen in (2.11) above, and with representative values $\tilde{\mu}^* = 0.1$ N s m^{-2}, $K^* = 1.6 \times 10^{-11}$ N, $h^* = 10^{-6}$ m, this corresponds to dimensional time $t^* = 0.156$ s.

2.2 Bistability and Switching

For a workable bistable device we require two distinct stable steady solutions in the absence of an electric field, and the ability to switch between these two states by transient application of an electric field. In §2.2.1 we demonstrate the existence of two such steady states, and in §2.2.2 we discuss how switching is investigated.

2.2.1 Stable, Field-free Steady States

The steady-state problem at zero field is particularly simple, reducing to

$$\theta_{zz} = 0, \qquad \theta_z = \pm\frac{\mathcal{A}_{\{0,1\}}}{2}\sin 2(\theta - \alpha_{\{0,1\}}) \quad \text{on } z = 0,\, 1. \tag{2.15}$$

Thus $\theta = az + b$, where the boundary conditions lead to coupled nonlinear equations for a and b. After simplification, two field-free solutions, which we call θ_1 and θ_2, are found:

$$\theta_1 = az + \frac{1}{2}\sin^{-1}\left(\frac{2a}{\mathcal{A}_0}\right) + \alpha_0, \tag{2.16}$$

$$\theta_2 = -az - \frac{1}{2}\sin^{-1}\left(\frac{2a}{\mathcal{A}_0}\right) + \alpha_0 + \pi, \tag{2.17}$$

where a must be found by numerically solving

$$a^2\left(1 + \frac{\mathcal{A}_1}{\mathcal{A}_0}\cos(2a + 2(\alpha_0 - \alpha_1))\right)^2 = \frac{\mathcal{A}_1^2}{4}\sin^2(2a + 2(\alpha_0 - \alpha_1)). \tag{2.18}$$

The solutions $\theta_{\{1,2\}}$ correspond to director fields $\boldsymbol{n}_{\{1,2\}} = (\sin\theta_{\{1,2\}}, 0, \cos\theta_{\{1,2\}})$. Equation (2.18) has multiple solutions for a in general, but in practice it is the smallest positive solution that gives the solutions $\boldsymbol{n}_{\{1,2\}}$ of lowest energy (the stablest solutions of the system).

2.2.2 Switching Investigation

With two steady field-free solutions found, we may now address the dynamic problem of how we might switch from one to the other and back again, by application of a transient electric field. That this is possible in certain parameter regimes was demonstrated by Cummings & Richardson [8], who studied a special case of the general model presented above. They found that when the anchoring angles are $\pi/2$ out-of-phase ($\alpha_1 = \alpha_0 - \pi/2$) and the anchoring strengths are the same at both boundaries ($\mathcal{A}_1 = \mathcal{A}_0$), two stable steady field-free states of equal energy exist, and

the states may be switched, reversibly, by application of a transient electric field. The two-way switching proved possible only for sufficiently small anchoring strength, however: in the case studied in [8] with $\alpha_0 = \pi/3$, switching was possible only when $\mathcal{A}_0 \lesssim 1.2$. This value may be rather small for robust device operation.[1]

Our strategy here is to consider the much more general model (2.12)–(2.14), with a specific "switching protocol": we suppose the system is in one of the two stable steady states at zero field, and then apply a constant electric field for a time period t_1, before decreasing the field linearly and continuously to zero over a subsequent time period t_2. Mathematically, this means that we solve the system (2.12)–(2.14) with initial condition $\theta(z,0) = \theta_{\{0,1\}}(z)$, and with variable field

$$\mathcal{F} = \mathcal{F}(t) = \begin{cases} \mathcal{F}_{\max} & 0 < t < t_1 \\ \frac{\mathcal{F}_{\max}}{t_2}((t_1+t_2) - t) & t_1 < t < t_1 + t_2 \\ 0 & t > t_1 + t_2. \end{cases} \tag{2.19}$$

Once the field has been removed, we continue the computation until the new zero-field equilibrium is reached. By the comment following (2.6), the parameter $\mathcal{D}$ that appears in the governing equation (2.12) is given by $\mathcal{D} = \mathcal{F}^2/\Upsilon$ (for constant dimensionless material parameter $\Upsilon = 10$), so is also a function of t. While we do not vary this basic switching protocol throughout our analysis, we consider $\mathcal{F}_{\max}$ and t_1 to be adjustable parameters, keeping the ratio t_1/t_2 fixed at 5. Following the justification given in §2.1, the anchoring strengths $\mathcal{A}_0$, $\mathcal{A}_1$, and the anchoring angles, α_0, α_1, are also taken as adjustable parameters. Switching occurs if the initial condition $\theta_{\{0,1\}}(z)$, by the end of the simulation, is transformed into $\theta_{\{1,0\}}(z)$. For a successful bistable device we require two-way switching.

[1]For example, as a minimum the surface anchoring must be strong enough that it is not disturbed by thermal fluctuations, yielding a condition $\mathcal{A} \gg k_B^* T^* h^*/(K^* S^*)$, where k_B^* is Boltzmann's constant, T^* is the absolute temperature of the system, and S^* is the effective cross-sectional area of the nematic molecule. Depending on the NLC used and the device size, this restriction can vary enormously, but for small NLC molecules could be prohibitive.

2.2.3 Optimization

Since we know from the results of [8] that two-way switching of the proposed bistable device is possible, our focus here is on finding the "best" possible such device. The question of what is best is not easy to answer, since a good bistable device should have several desirable properties. The properties we consider are:

- The device should be robust. A key feature here is that the energy wells of the free energy minima should be reasonably deep. This includes the surface energy contributions; so the dimensionless surface energies $\mathcal{A}_{\{0,1\}}$ should not be too small. (The upper bound of 1.2 found in the previous analysis is likely prohibitively small; a device with such low surface energies could be prone to undesired switching, *e.g.* if the device was jolted.)

- Two-way switching should be possible at relatively low electric field strengths. Thus, given a value of the material parameter Υ, the value $\mathcal{F}_{\max}$ of the applied switching field should not be too large.

- The two steady states $\boldsymbol{n}_1$ and $\boldsymbol{n}_2$ should be optically-distinct. Therefore, the two solutions found should be sufficiently "different" in some suitable measure, which we take as an approximation of the difference in optical transmission of the two states when the layer is placed between crossed polarizers.

- The time taken to switch from one stable state to the other should be as short as possible.

These conditions are conflicting, to a certain extent, so some design decisions have to be made as to which are more important. The approach we take is to define a "benefit function" B, which takes account of each of the above criteria. We define

$$B = \begin{cases} \min\{A_0, A_1\} + \mu C(\boldsymbol{n}_1, \boldsymbol{n}_2) & \\ -\nu|\mathcal{F}_{\max}| - \gamma(t_1 + t_2) & \text{if 2-way switching occurs,} \\ 0 & \text{otherwise,} \end{cases} \tag{2.20}$$

where $C(\boldsymbol{n}_1, \boldsymbol{n}_2)$ is a contrast function defined below, and seek to maximize this function.[2] The first term in B ensures that surface energies will be as large as possible (subject to the other constraints); the second term maximizes contrast between the two stable states found; the third term minimizes the field strength at which the two-way switching occurs; and the fourth term minimizes the length of time for which the electric field is applied.

The weight factors μ, ν and γ are chosen at our discretion, and allow for adjustment of the weight of each of the terms in B in order to emphasize different desired properties: for example, if fast switching is considered of paramount importance then a large value for γ should be used; while if high contrast is more important then a large value for μ should be used. Optimization of B for given values of μ, ν and γ is a computationally-intensive process, requiring a search through $(\mathcal{A}_0, \mathcal{A}_1, \alpha_0, \alpha_1, \mathcal{F}_{\max}, t_1)$ parameter space (recall that we set $t_1/t_2 = 5$ throughout our simulations) in order to determine where two-way switching occurs, and if so, what the corresponding value of B is.

The Contrast Function $C(\boldsymbol{n}_1, \boldsymbol{n}_2)$

Our contrast function is based on the difference in optical transmission of our two solutions. Recall that we are solving for the director angle θ numerically in our time-dependent simulations, so that we obtain a discretized solution $\{\theta_j\}_{j=1}^{N}$ on our mesh of size N. For a given discretized solution we obtain the optical transmission between crossed polarizers as follows: The retardation δ for a given director configuration is

[2]Note: In principle the function B defined in (2.20) could assume negative values at some points of parameter space, in which case the value zero in its definition could easily be replaced by some suitable negative number. This did not occur in any of our simulations.

defined by [31]

$$\begin{aligned}\delta &= \frac{2\pi n_o}{\lambda_0^*}\int_0^{h^*}\left[\frac{1}{\sqrt{1-\dfrac{n_e^2-n_o^2}{n_e^2}\sin^2\theta(z^*)}}-1\right]dz^* \\ &= \frac{2\pi n_o h^*}{\lambda_0^*}\int_0^{1}\left[\frac{1}{\sqrt{1-\dfrac{n_e^2-n_o^2}{n_e^2}\sin^2\theta(z)}}-1\right]dz\end{aligned}$$

where n_o and n_e are the ordinary and extra-ordinary refractive indices and λ_0^* the wavelength in vacuo. In order to obtain a somewhat more general expression for the contrast function (see below) we use the small birefringence approximation, $n_e/n_o - 1 \ll 1$ (the value for a fairly typical liquid crystal that might be used in applications is around 0.13), to evaluate δ for each steady state, which leads to

$$\delta \approx \frac{\varepsilon^2\pi n_o h^*}{\lambda_0^*}\int_0^1 \sin^2\theta(z)\,dz \approx \frac{\varepsilon^2\pi n_o h^*}{\lambda_0^* N}\sum_{j=1}^{N}\sin^2\theta_j, \quad \varepsilon^2 = 1-\frac{n_o^2}{n_e^2} \ll 1.$$

We then use this expression to evaluate the transmission T [31],

$$T = \sin^2(\delta/2). \tag{2.21}$$

Using a further small δ approximation (again based on the smallness of ε^2) this gives $T \approx (\delta/2)^2$, thence

$$T \approx \left(\frac{\varepsilon^2\pi n_o h^*}{2\lambda_0^* N}\sum_{j=1}^{N}\sin^2\theta_j\right)^2 = \text{constant} \times \left(\sum_{j=1}^{N}\sin^2\theta_j\right)^2. \tag{2.22}$$

This approximation, while not as accurate as evaluating the transmission according to the exact definition, has the advantage that we do not need to specify the refractive indices when evaluating T, so the results are somewhat more general. Finally then, in our numerical implementation, we define the contrast function $C(\boldsymbol{n}_1, \boldsymbol{n}_2)$ in (2.20)

by the following expression, proportional to the difference in optical transmissions of the two states θ_1, θ_2:

$$C(\boldsymbol{n}_1, \boldsymbol{n}_2) = \left| \left(\sum_{j=1}^{N} \sin^2 \theta_{1,j} \right)^2 - \left(\sum_{j=1}^{N} \sin^2 \theta_{2,j} \right)^2 \right|.$$

2.3 Optimization: Numerical Method and Results

As indicated above, our task is to search through the parameter space ($\mathcal{A}_0, \mathcal{A}_1, \alpha_0, \alpha_1, \mathcal{F}_{\max}, t_1$) of anchoring strengths, anchoring angles, switching field and switching time, to determine whether two-way switching occurs and, if it does, which point in parameter space maximizes the benefit function B defined in (2.20). Since the benefit function is time-consuming to evaluate, and parameter space is large, we implement a simulated annealing method [1] to achieve the maximization. Due to the complexity of the full problem, we approach it in stages.

1. As a simple test case we first maximize B when $\nu = \gamma = 0$. We fix $\alpha_1 = \alpha_0 - \pi/2$ (but α_0 can vary); $|\mathcal{F}_{\max}|$ and t_1 are also fixed, but $\mathcal{F}_{\max}$ can be of either sign. Here the optimization is carried out in 3D ($\alpha_0, \mathcal{A}_0, \mathcal{A}_1$) parameter space.

2. We next allow α_1 to vary independently, and search optima in 4D ($\alpha_0, \alpha_1, \mathcal{A}_0, \mathcal{A}_1$) parameter space.

3. Next allow $\nu > 0$ in B and minimize the switching field strength also.

4. Finally, we allow $\gamma > 0$ and take switching time into account too.

In all cases we use a simulated annealing method to maximize the benefit function B [1]. This is a gradient method with a certain stochastic character, represented by a "temperature" T. An initial simplex in parameter space is required to start the method ($(n+1)$ initial points specified in an n-dimensional parameter space). The system is "cooled" from an initial state, and the "temperature" T at any stage

captures the probability that the method can move down gradients in B as well as up. The Boltzmann probability distribution,

$$\text{Prob}(E) \sim \exp(-E/kT)$$

expresses the idea that a system in thermal equilibrium at temperature T has its energy probabilistically distributed among all different energy states E. Even at low temperature, there is a chance, albeit very small, of a system being in a high energy state. Therefore, there is a corresponding chance for the system to get out of a local energy maximum in favor of finding a better, more global, one. The quantity k (Boltzmann's constant) is a constant of nature that relates temperature to energy. In other words, the system sometimes goes down as well as up; but the lower the temperature, the less likely is any significant down excursion. At zero temperature, the method has no stochastic element, and goes always up gradients, which is equivalent to the simplex method [1]. There is a certain amount of choice in the method's implementation: firstly in the choice of so-called annealing schedule (how the system is cooled); and secondly, in the choice of initial simplex to start the method. To deal with the dependence on initial conditions we perform the optimization for a random selection of initial simplices, and make a histogram of the results. We plot the value of the benefit function attained for each implementation of simulated annealing (in an ideal implementation of simulated annealing this should always be the global optimum) against the number of initial simplices that converge to this value. The best results obtained are supposed to be the global optimum of B, and in general we see that this optimum corresponds to, or is close to, the dominant spike in the histogram, indicating reasonable robustness of the simulated annealing method. Regarding the annealing schedule, it is known that slower cooling produces more accurate results; however, it also increases the computational time. We carried out preliminary numerical experiments to find an annealing schedule that is accurate,

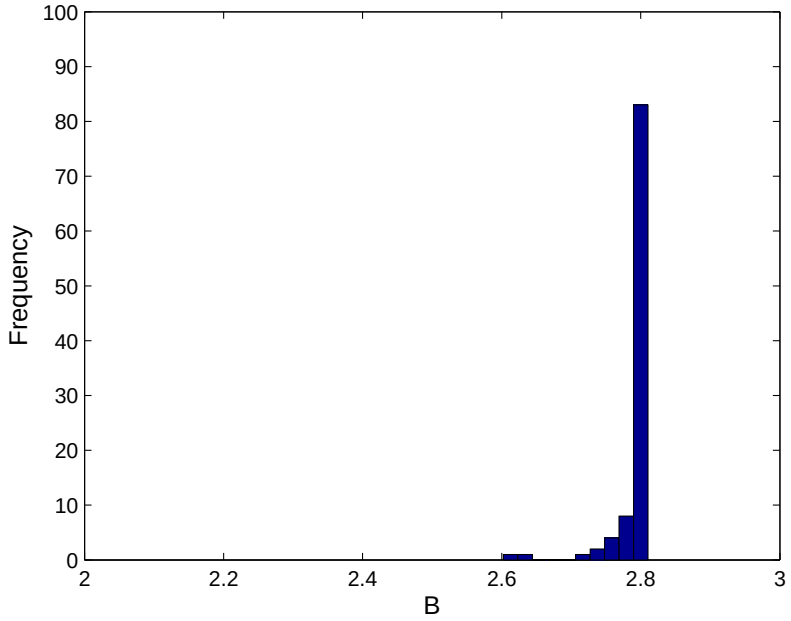

Figure 2.4 Histogram showing the optimization for the benefit function B (2.20), with $\mu = 1.0, \nu = 0, \gamma = 0$, in 3D $(\mathcal{A}_0, \mathcal{A}_1, \alpha_0)$-parameter space for 100 different initial simplices. Note that the dominant spike in the value of B corresponds to the largest value attained.

but that still allows us to obtain the results with reasonable use of computational resources.

2.3.1 Optimization: 3D Results

In the simulations of Cummings & Richardson [8], the same model (2.12)–(2.14) was considered, with electric field specified by (2.19). However in [8] a very limited device design was considered: it was assumed that (i) anchoring angles differ by $\pi/2$ (that is, $\alpha_1 = \alpha_0 - \pi/2$); (ii) α_0 was fixed at $\pi/3$; (iii) surface energies were equal, $\mathcal{A}_1 = \mathcal{A}_0$; (iv) the dimensionless switching field strength $|\mathcal{F}_{\max}|$ in (2.19) was fixed at 5; and (v) the dimensionless parameters t_1 and t_2 characterizing total switching time in (2.19) were fixed by $t_1 = 25$, $t_2 = 5$. Our first step towards generalizing and improving on these results is to allow different surface energies on each bounding surface and, while keeping $\alpha_1 = \alpha_0 - \pi/2$, allow the anchoring angle α_0 to vary freely. Other parameters

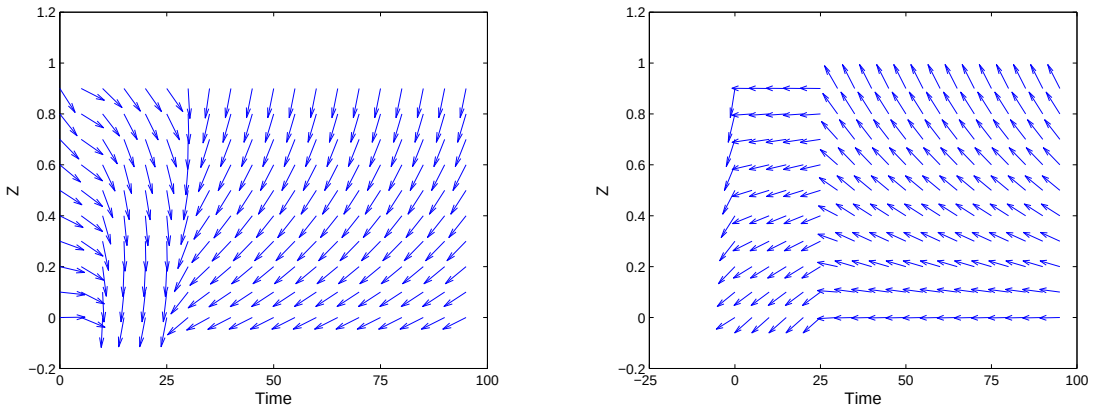

Figure 2.5 Switching simulations $\boldsymbol{n}_1$ to $\boldsymbol{n}_2$ (left) and $\boldsymbol{n}_2$ to $\boldsymbol{n}_1$ (right), for the optimal benefit function parameters $\mathcal{A}_0 = 5.0$, $\mathcal{A}_1 = 2.4$ and $\alpha_0 = 1.36$. Dimensionless time runs along the horizontal axis, and the director field is displayed at equally-spaced time intervals. The field is applied to $\boldsymbol{n}_1$ (or $\boldsymbol{n}_2$) at $t = 0$, maintained at a constant level until $t = 25$, and then decreased linearly to zero over the next 5 time units.

are taken as listed above (see [8] for full details). We then seek to maximize the benefit function B as defined by (2.20) with $\nu = \gamma = 0$, as $\mathcal{A}_0$, $\mathcal{A}_1$ and α_0 vary. We carry out simulated annealing over this 3D parameter space as explained above, for 100 different (random) choices of initial simplex (four starting points in $(\mathcal{A}_0, \mathcal{A}_1, \alpha_0)$-space).

The histogram of the results is shown in Figure 2.4: from this we conclude that the optimum value of B here is about 2.82. It is possible in principle that different points in parameter space correspond to the same value of B, but it turns out that all 80-plus simulations that converge to this dominant optimum correspond to essentially the same parameter values: $\mathcal{A}_0 = 5.0$, $\mathcal{A}_1 = 2.4$ and $\alpha_0 = 1.36$. These values may be compared to the results of [8], where it was found that, with the restrictions (i)-(v) outlined above, the largest value of $\mathcal{A}_0 = \mathcal{A}_1$ that permits two-way switching is 1.21, with $\alpha_0 = \pi/3 = 1.047$. Therefore even this simple generalization has resulted in a two-fold improvement in the operating values of surface energies, with associated implications for device robustness. For the simulations shown here, the parameter μ was chosen as $\mu = 1.0$; for this value the two nonzero terms in the benefit function

B are approximately the same size, and so are considered as being of roughly equal importance. For these parameter choices we can compute the so-called *contrast ratio* of the two steady states found, that is, the ratio of the transmission coefficients for each steady state (a widely-used measure of contrast in LCDs; the ratio is always taken such that it is greater than or equal to one), and it evaluates to 3.11 using our approximation (2.22) (the exact value computed using typical values of refractive indices, wavelengths, etc. is within 10% of this value). Different choices of the weight parameter μ will presumably change this result somewhat; we discuss the sensitivity to the choice of μ in §2.3.2 below.

The switching simulations for the optimal parameter values found are shown in Figure 2.5, for both cases $\boldsymbol{n}_1$ to $\boldsymbol{n}_2$, and vice-versa. It appears that after application of the electric field the new "constant applied field" equilibrium state is obtained rapidly in both cases. This suggests that the field could be removed sooner and switching would still occur. However, numerical tests indicate that while this is possible for $\boldsymbol{n}_1$ to $\boldsymbol{n}_2$ switching, switching from state $\boldsymbol{n}_2$ to $\boldsymbol{n}_1$ is a more difficult process, and is the limiting factor when minimizing total switching time (see §2.3.4 and §2.3.5 later). We do not, in this thesis, consider the more complicated (and likely impractical) scenario of allowing different switching protocols for the two switching directions (though in principle one could save energy by so doing).

2.3.2 Optimization: 4D Results

The next step is to allow α_1 to vary independently of α_0, but keep other parameters fixed as outlined in §2.3.1. We again implement simulated annealing to maximize B, with $\nu = \gamma = 0$ in (2.20), but in 4D $(\mathcal{A}_0, \mathcal{A}_1, \alpha_0, \alpha_1)$-parameter space. The annealing method now requires five initial points (an initial simplex) in the 4D parameter space to begin the iteration; since results in general may depend on the choice of initial simplex, we use 100 different initial simplices as in §2.3.1 above and make a histogram

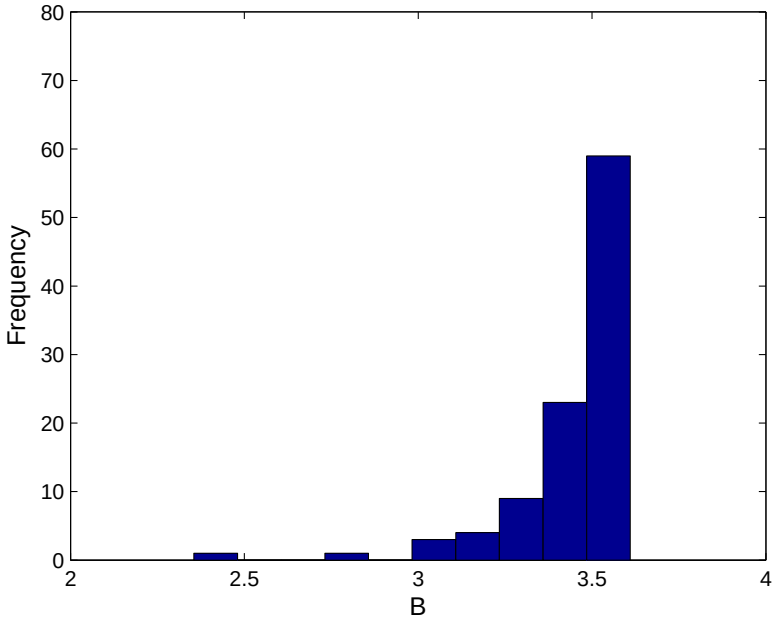

Figure 2.6 Histogram showing the optimization for the benefit function B (2.20), with $\mu = 0.1, \nu = 0, \gamma = 0$, in 4D $(\mathcal{A}_0, \mathcal{A}_1, \alpha_0, \alpha_1)$-parameter space for 100 different initial simplices. Note that the dominant spike in the value of B corresponds to the largest value attained. Other spikes could be local optima.

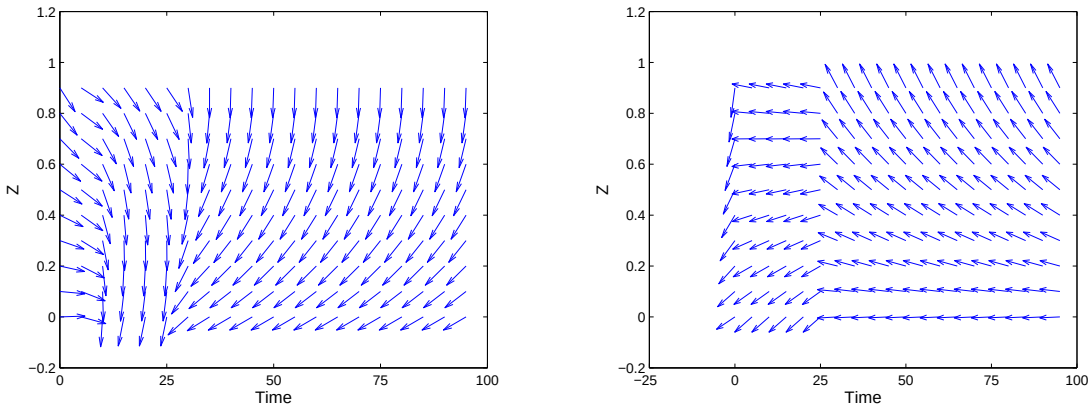

Figure 2.7 Switching simulations $\boldsymbol{n}_1$ to $\boldsymbol{n}_2$ (left) and $\boldsymbol{n}_2$ to $\boldsymbol{n}_1$ (right) for the optimal benefit function parameters of §2.3.2, $\mathcal{A}_0 = 4.92$, $\mathcal{A}_1 = 3.20$, $\alpha_0 = 1.34$ and $\alpha_1 = -0.33$. Dimensionless time runs along the horizontal axis, and the director field is displayed at equally-spaced time intervals. The field is applied to $\boldsymbol{n}_1$ (or $\boldsymbol{n}_2$) at $t = 0$, maintained at a constant level until $t = 25$, and then decreased linearly to zero over the next 5 time units.

of the results for the optimization in each case. The resulting histogram is shown in Figure 2.6. There is more scatter in the optimization results this time, as we would expect in a larger parameter space; nonetheless a clear optimum emerges, which is again the largest spike in the distribution. From these results, we conclude that the optimum value of B here is about 3.55. Again, all optimization results that lie within the dominant spike are found to correspond to (more or less) the same point in parameter space: $\mathcal{A}_0 = 4.97$, $\mathcal{A}_1 = 3.20$, $\alpha_0 = 1.35$ and $\alpha_1 = -0.33$. Since the smaller surface energy is increased from the previous case above, we have improved robustness (as we would expect, since we simply relaxed a constraint on the system). Switching simulations for the optimal parameter values are shown in Figure 2.7. As before, we can evaluate the contrast ratio for the two "optimal" steady states, and it evaluates to 3.59.

Perhaps surprisingly, the key results do not appear to be very sensitive to the value chosen for μ (the weight associated with the contrast term in the benefit function). Table 2.1 shows how the optimal points in parameter space, and the corresponding value of the benefit function B, depend on the value of μ. Only the value of B changes significantly, due to the direct appearance of μ in its definition. As μ varies by a factor of 4, the lower of the two surface energies varies by only a small amount in value. Therefore, we present only the histogram of results for the single value $\mu = 1.0$ in Figure 2.6 (this is also the value of μ at which the two terms in B are roughly the same size). The value of μ is fixed at 1.0 for the remainder of the paper.

2.3.3 Optimization: 5D Results, Part 1

We now extend our investigation to allow the "switching field" $\mathcal{F}_{\max}$ to vary also, thus we allow $\nu > 0$ in the benefit function (2.20). This is the first stage at which we expect to see the effects of compromise in our optimization – since we now seek to

Table 2.1 The Optimal Points with Parameter Values and Corresponding Benefit Function Values Dependence on μ

μ	$\mathcal{A}_0$	$\mathcal{A}_1$	α_0	α_1	B
1.0	4.97	3.20	1.35	-0.33	3.61
2.0	4.83	3.18	1.34	-0.34	4.02
3.0	4.54	3.12	1.32	-0.35	4.45
4.0	4.27	3.05	1.31	-0.36	4.91

decrease the size of the switching field, we may anticipate a corresponding decrease in the allowable surface energies at which switching can occur (a smaller field can generate less force on the NLC molecules, hence only weak anchoring can be broken).

Figure 2.8 shows the results of 100 simulated annealing computations to maximize B, with $\mu = 1.0$, $\nu = 0.1$, $\gamma = 0$ in (2.20). Figures 2.9 and 2.10 illustrate smaller ($\nu = 0.05$) and larger ($\nu = 0.3$) ν-values, respectively. The representative values of Figure 2.8 were chosen, as before, so as to give an approximate balance between terms in the benefit function, "robustness", contrast and low switching field all being considered of roughly equal importance. The left-hand subfigure in each case is the usual histogram of results (converged value of B versus frequency), while the right-hand subfigure shows a scatter plot of the corresponding switching field for each simulated annealing result, along with the corresponding surface energies $\mathcal{A}_0$ and $\mathcal{A}_1$. Note that the largest value of B obtained is, in all cases, no longer the dominant spike in the histogram. The simulated annealing method is designed to converge to the global optimum of the given function and performed well in this regard for the 3D and 4D cases of §2.3.1, §2.3.2; here it does less well and more often converges to sub-optimum values of B. Since this increased scatter occurs for the benefit

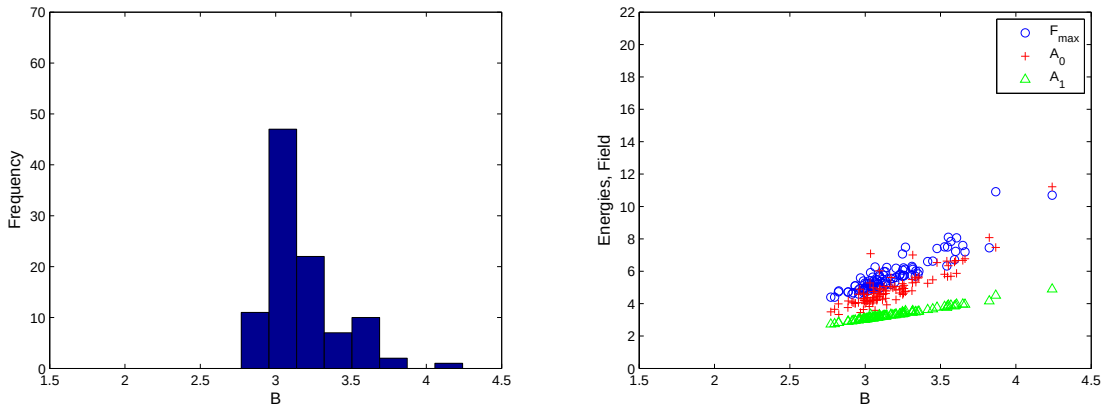

Figure 2.8 Histogram of B-values and scatter plot of switching fields $|\mathcal{F}_{\max}|$ and associated surface energies from the simulated annealing optimization of the benefit function B (2.20), with $\mu = 1.0, \nu = 0.1, \gamma = 0$, in $(\mathcal{A}_0, \mathcal{A}_1, \alpha_0, \alpha_1, \mathcal{F}_{\max})$-parameter space. 100 different initial simplices were used.

function which, for the first time, includes competing effects, we conjecture that these competing terms lead to a much more complicated structure of the landscape defined by the benefit function, with several local optima, making the finding of global optima much more demanding. We expect in this case that implementing a sufficiently slow 'cooling' schedule would allow us to converge to the global optimum more often; however, currently available computational resources do not allow us to explore this issue fully in such a large parameter space (we did repeat the simulations of Figure 2.8 with a cooling schedule that was twice as slow, and obtained qualitatively very similar results, not reproduced here). Therefore we compromise to a certain degree and assume that the data points in the right-most spike of the histograms represent the global optimum of B, while other converged simulations represent local optima (it was verified directly for several cases that converged values of the benefit function are indeed local maxima).

As usual, what is of interest is not the numerical value of B when maximized, but the corresponding values of the optimal parameters; and as noted above, with competing terms in the benefit function B we see evidence of multiple maxima. From

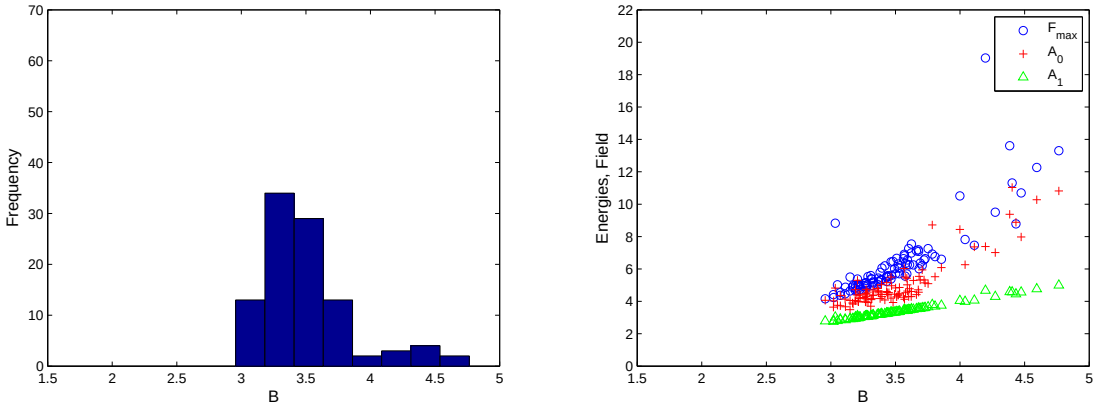

Figure 2.9 As for Figure 2.8, but with $\nu = 0.05$.

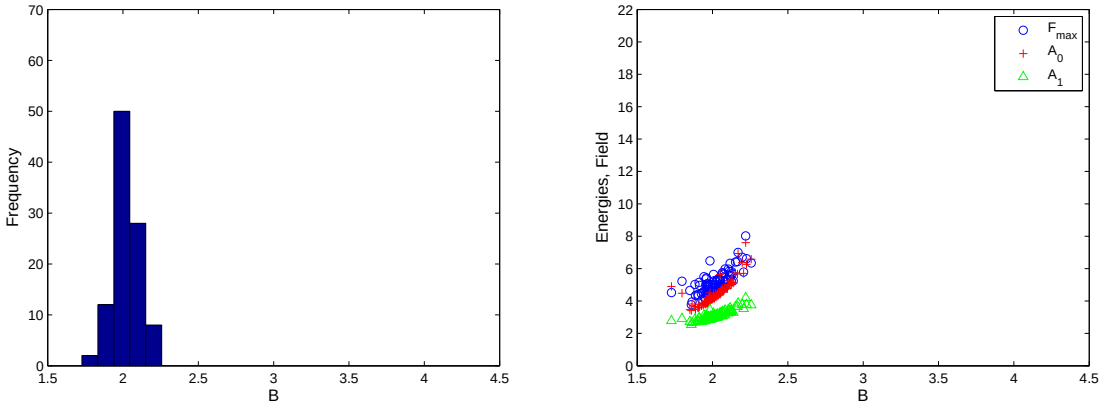

Figure 2.10 As for Figure 2.8, but with $\nu = 0.3$.

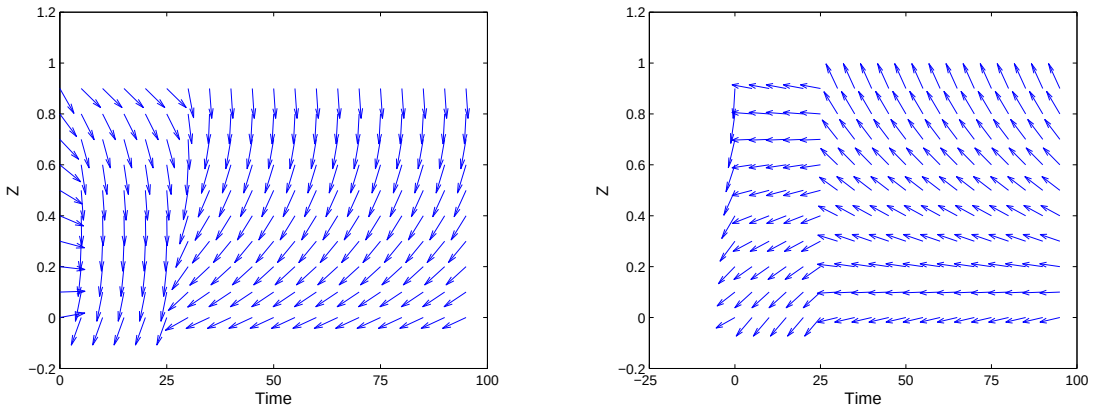

Figure 2.11 Switching simulation (a) $\boldsymbol{n}_1$ to $\boldsymbol{n}_2$ and (b) $\boldsymbol{n}_2$ to $\boldsymbol{n}_1$, for optimal benefit function parameters for the case $\mu = 1.0$, $\nu = 0.1$ ($\mathcal{A}_0 = 11.22$, $\mathcal{A}_1 = 4.89$, $\alpha_0 = 1.32$, $\alpha_1 = -0.35$, $\mathcal{F}_{\max} = -10.69$). Dimensionless time runs along the horizontal axis, and the director field is displayed at equally-spaced time intervals. The field is applied to $\boldsymbol{n}_1$ (or $\boldsymbol{n}_2$) at $t = 0$, maintained at a constant level until $t = 25$, and then decreased linearly to zero over the next 5 time units.

the scatter plots in Figures 2.8, 2.9 and 2.10 for example we see that, although a rare event, the simulated annealing algorithm can converge to the same value of B but with different switching fields $\mathcal{F}_{\max}$, corresponding to multiple device designs that (according to our chosen measure) are "equally optimal". Unsurprisingly, we find that the larger $\mathcal{F}_{\max}$ "optima" (local, not global) are associated with larger surface energies $\mathcal{A}_0$, $\mathcal{A}_1$, while smaller $\mathcal{F}_{\max}$ "optima" (again, non-global) are associated with smaller surface energies. These findings reflect the fact that, if we want a device with large surface energies then we require a larger field to break the surface anchoring and switch; and vice-versa, if we want switchability at low fields then anchoring strengths cannot be too large.

By changing the weight ν associated with the switching field in the benefit function (2.20) we can alter the results somewhat, though the same general conclusions emerge. Figures 2.9 and 2.10 show the results for smaller and larger values, $\nu = 0.05$ and $\nu = 0.3$, respectively. In the former case, less value is placed on having a low switching field, and we find that the simulated annealing tends to converge to

B-values with higher fields $\mathcal{F}_{\max}$, and higher surface energies. In the latter case, the higher weight associated with $\mathcal{F}_{\max}$ says that low switching fields are valued more, and indeed, the simulated annealing now converges to B-values that are associated with significantly lower values of $\mathcal{F}_{\max}$ (though, of course, lower surface energies also). All the scatter plots are shown on the same axes for ease of comparison.

Figure 2.11 shows the two-way switching simulations corresponding to the optimum value of B obtained from the scatter plot of Figure 2.8. The left-hand subplot shows the switching $\boldsymbol{n}_1$ to $\boldsymbol{n}_2$, while the right-hand subplot shows the switching $\boldsymbol{n}_2$ to $\boldsymbol{n}_1$ for this optimum, as detailed in the caption. The contrast ratio associated with these two steady states was evaluated to be 3.55.

2.3.4 Optimization: 5D Results, Part 2

The final consideration that we wish to take into account is the total time taken to switch. Since we observe that the NLC rapidly relaxes to a zero field equilibrium once the electric field is removed, we measure switching time simply by the time for which the electric field must be applied, and we seek to minimize this. In the first instance, we revert to the fixed-field-strength case, $|\mathcal{F}_{\max}| = 5$, and seek to optimize B (with $\nu = 0$, $\mu, \gamma > 0$) in $(\mathcal{A}_0, \mathcal{A}_1, \alpha_0, \alpha_1, t_1)$-parameter space. When doing so, the time t_2 over which the field is decreased to zero is fixed at $t_1/5$ in (2.19), consistent with the previous cases.

Figure 2.12 shows the usual histogram of results and a scatter plot of switching times and surface energies for the results of 100 simulated annealing computations to maximize B, with $\mu = 0.1$, $\gamma = 0.02$, $\nu = 0$ in (2.20). Figures 2.13 and 2.14 illustrate smaller ($\gamma = 0.01$) and larger ($\gamma = 0.03$) γ-values, respectively. Again, these representative γ-values were chosen so as to give an approximate balance of terms in the benefit function. Once more we see the possibility of multiple (local) maxima in the benefit function. In Figure 2.12, we see an apparent global optimum, at the far

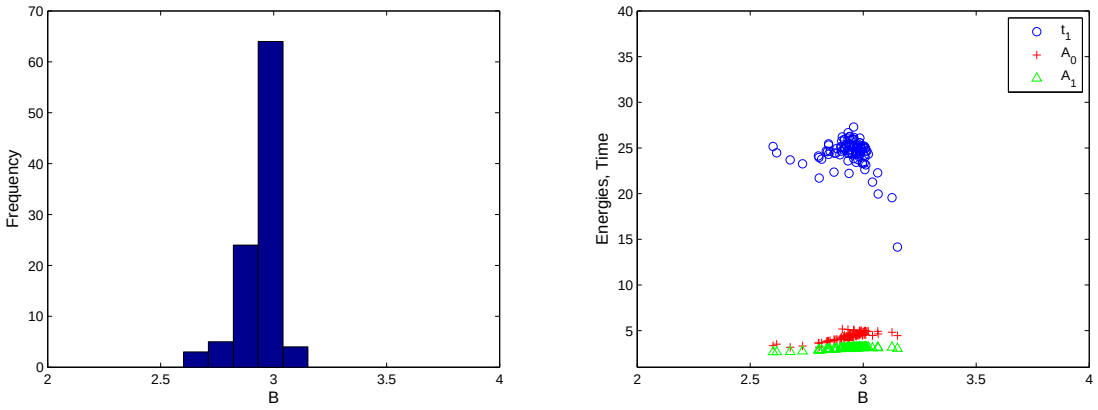

Figure 2.12 Histogram of B-values and scatter plot of switching times t_1 and associated surface energies from the simulated annealing optimization of the benefit function B (2.20), with $\mu = 1.0, \nu = 0, \gamma = 0.02$, in 5D $(\mathcal{A}_0, \mathcal{A}_1, \alpha_0, \alpha_1, t_1)$-parameter space. 100 different initial simplices were used.

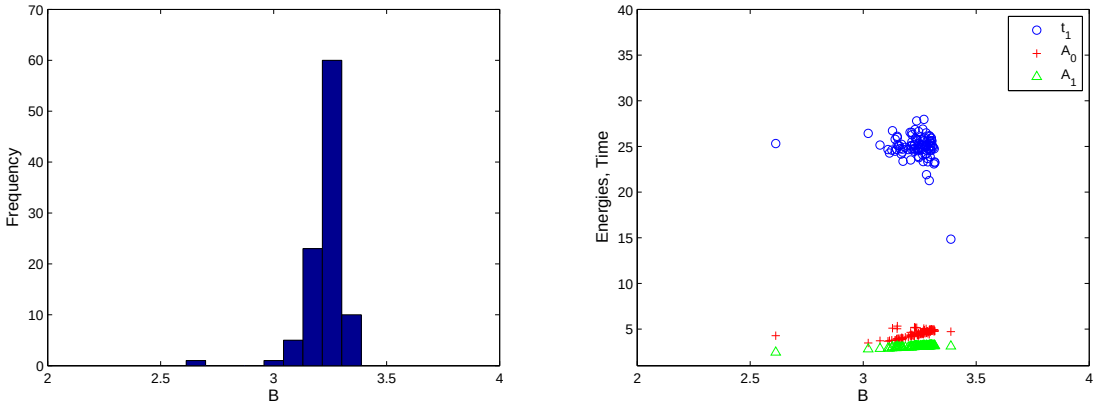

Figure 2.13 As for Figure 2.12, but with $\gamma = 0.01$.

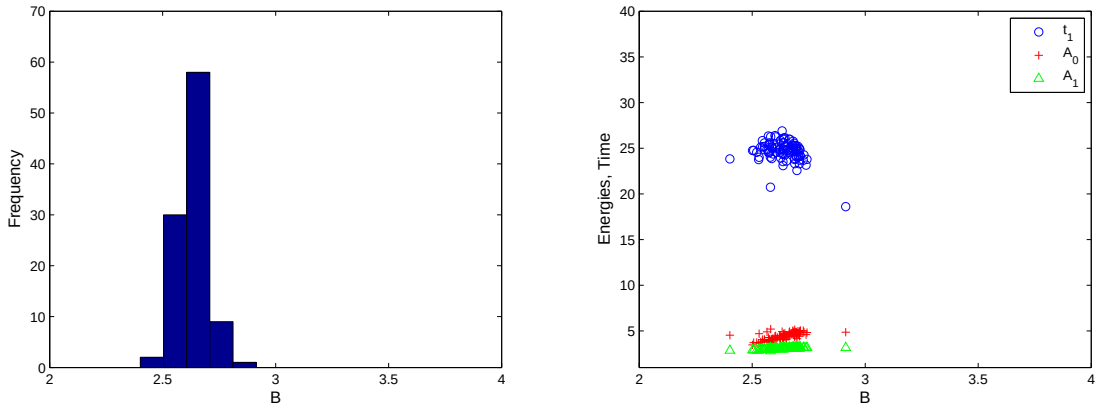

Figure 2.14 As for Figure 2.12, but with $\gamma = 0.03$.

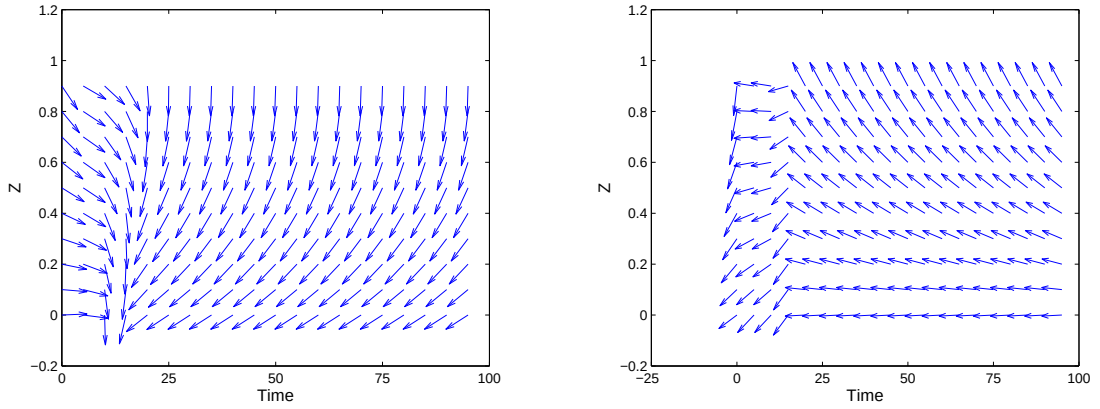

Figure 2.15 Switching simulation (a) $\boldsymbol{n}_1$ to $\boldsymbol{n}_2$ and (b) $\boldsymbol{n}_2$ to $\boldsymbol{n}_1$ for optimal benefit function parameters for the case $\mu = 1.0$, $\nu = 0$, $\gamma = 0.02$ ($\mathcal{A}_0 = 4.47$, $\mathcal{A}_1 = 3.04$, $\alpha_0 = 1.32$, $\alpha_1 = -0.34$, $t_1 = 14.15$). Dimensionless time runs along the horizontal axis, and the director field is displayed at equally-spaced time intervals. The field is applied to $\boldsymbol{n}_2$ at $t = 0$, maintained at a constant level until $t = t_1$, and then decreased linearly to zero over the next $t_1/5$ time units.

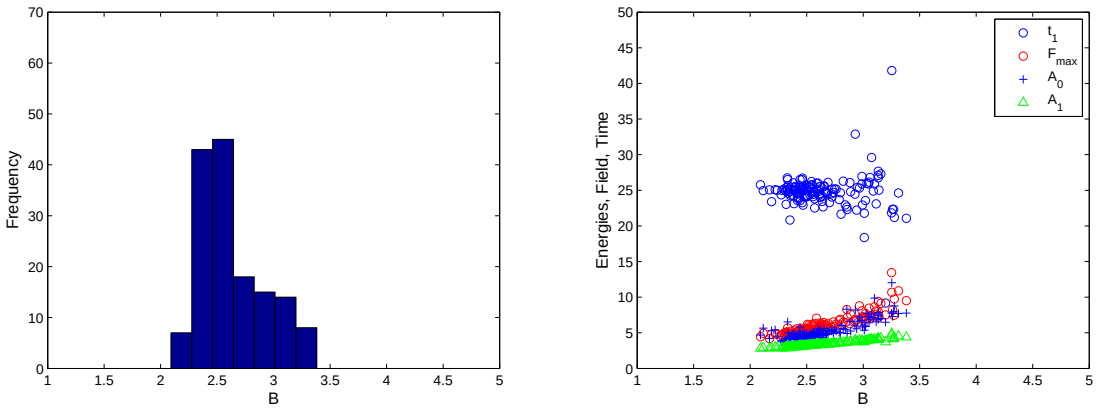

Figure 2.16 Histogram of B-values and scatter plot of switching times t_1, switching fields $|\mathcal{F}_{\max}|$ and associated surface energies $\mathcal{A}_0$, $\mathcal{A}_1$ from the simulated annealing optimization of the benefit function B (2.20), with $\mu = 1.0, \nu = 0.1, \gamma = 0.02$, in 6D $(\mathcal{A}_0, \mathcal{A}_1, \alpha_0, \alpha_1, \mathcal{F}_{\max}, t_1)$-parameter space. 150 different initial simplices were used.

right of the scatter plot. Two-way switching simulations for the parameters associated with this lowest-switching time solution are given in Figure 2.15; the contrast ratio associated with these solutions is evaluated as 4.14. As expected, the global optimum solution, though it has the shortest switching time ($t_1 = 14.15$), allows for higher surface energies than suboptimal solutions (local maxima of B). With the parameter values quoted at the end of §2.1.2, this corresponds to a dimensional switching time of around 88 ms which, while rather slow for a conventional (high power) LCD, is certainly competitive with the switching times of e-ink based devices. Note also that this time could be reduced further by choosing a larger value for the parameter γ in the benefit function.

2.3.5 Optimization: 6D Results

To take all aforementioned effects into account simultaneously in our optimization we must work with the full benefit function B with all parameters $\mu, \nu, \gamma \neq 0$, and maximize it in 6D $(\mathcal{A}_0, \mathcal{A}_1, \alpha_0, \alpha_1, \mathcal{F}_{\max}, t_1)$-parameter space. As before, the results of the optimization will depend to a certain extent on the values chosen for μ, ν

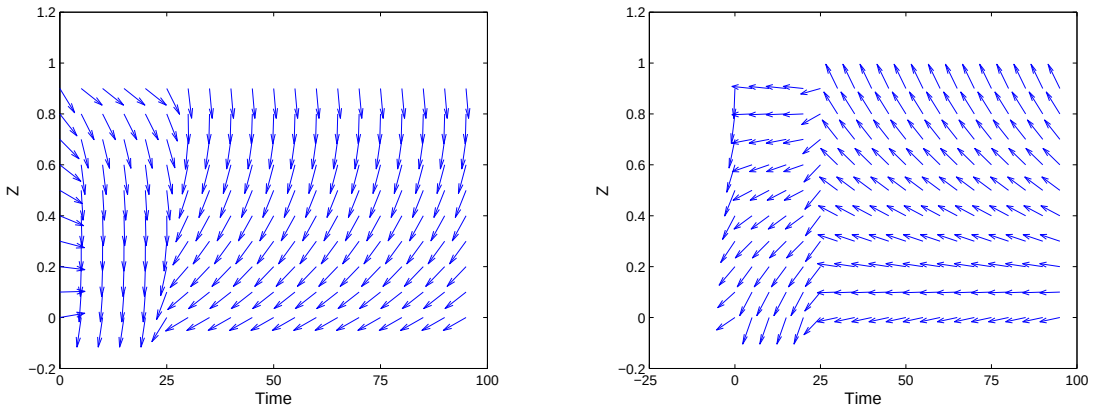

Figure 2.17 Switching simulations $\boldsymbol{n}_1$ to $\boldsymbol{n}_2$ (left) and $\boldsymbol{n}_2$ to $\boldsymbol{n}_1$ (right) for optimal benefit function parameters for the case $\mu = 1.0$, $\nu = 0.1$, $\gamma = 0.02$ ($\mathcal{A}_0 = 7.72$, $\mathcal{A}_1 = 4.54$, $\alpha_0 = 1.30$, $\alpha_1 = -0.37$, $\mathcal{F}_{\max} = -10.90$, $t_1 = 24.62$). Dimensionless time runs along the horizontal axis, and the director field is displayed at equally-spaced time intervals. The field is applied to $\boldsymbol{n}_1$ (or $\boldsymbol{n}_2$) at $t = 0$, maintained at a constant level until $t = t_1$, and then decreased linearly to zero over the next $t_1/5$ time units.

and γ, and these values may be adjusted depending on the particular attributes we wish to emphasize. We present just one illustrative example here, with $\mu = 1.0$, $\nu = 0.1$, $\gamma = 0.02$. Figure 2.16 shows the histogram of results for the simulated annealing algorithm as applied to 150 different, randomly-chosen, initial simplices in our 6D parameter space, along with a scatter plot showing where in parameter space each of the converged simulated annealing results lies. We present also switching simulations $\boldsymbol{n}_1$ to $\boldsymbol{n}_2$ and $\boldsymbol{n}_2$ to $\boldsymbol{n}_1$ in Figure 2.17, for the optimal parameter values found (corresponding to the largest value of B in Figure 2.16, $B \approx 3.45$). The contrast ratio associated with the two steady states of Figure 2.17 is evaluated as 4.23.

2.4 Discussion and Conclusions of 1D Case

We have presented a study of a very simple theoretical bistable nematic Liquid Crystal Display (LCD) device, consisting of a nematic sandwich, bounded by planar surfaces at which anchoring properties can be controlled. Regarding these anchoring properties (angles and strengths) as independent design parameters, we posed the

question: which set of anchoring properties gives the "best" such device? Formulating this question mathematically, setting up the machinery whereby the design may be optimized according to specific preferred features, and presenting several examples of such optimization which (we believe) bring closer the realization of such a bistable device, are the basis of the work in this chapter.

Several criteria were taken into consideration when deciding what makes a "good" device. From the point of view of design, a device is specified in our dimensionless model by choices of anchoring angles α_0, α_1, dimensionless anchoring strengths $\mathcal{A}_0$, $\mathcal{A}_1$, and the dimensionless material parameter $\Upsilon = \mathcal{F}^2/\mathcal{D}$ defined in (2.7). (Obviously, the various dimensional physical quantities such as the "bend" elastic constant of the chosen nematic, the nematic layer thickness h^*, and so on, all appear in the definitions of our dimensionless parameters.) As a minimum, a workable device must be switchable (both ways) for some choice of applied electric field, and manufacturable at physically-attainable values of α_0, α_1, $\mathcal{A}_0$, $\mathcal{A}_1$ and Υ. A good device should have several additional desirable properties however, chiefly, those listed in §2.2.3. In order to optimize these desirable properties, we introduced our benefit function B, defined in (2.20), and searched through the space of switchable devices in order to maximize B.

Given the properties we wish to optimize simultaneously, it is natural that some tradeoff is necessary. This becomes particularly apparent when we carry out the optimization in stages, introducing one desirable quantity at a time. When we optimize only by maximizing the allowable surface energies (with implications for device robustness) and the optical contrast, dimensional surface energies that are both in excess of $3.2 \times K^*/h^*$ (where $K^* = K_1^* = K_3^*$ is the elastic energy of the liquid crystal and h^* is the thickness of the nematic layer in the proposed device) are attainable. With, for example, representative values $K^* = 1.6 \times 10^{-11}$ N, $h^* = 10^{-6}$ m, this corresponds to surface energy $A^* = 5.1 \times 10^{-5}$ N m^{-1}, a fairly respectable value

in terms of manufacturing attainability and robustness of the steady states to shocks. However, when we also consider minimizing the switching field (measured by the dimensionless quantity $\mathcal{F}_{\max}$) and/or the switching time, the allowable surface energies fall, to an extent that depends on how much weight we attach to each desirable property. Figures 2.8–2.10 and 2.12–2.14 exemplify this tradeoff, showing clearly that higher surface energies require higher switching fields in general, and longer switching times. We emphasize that our optimization is carried out for our dimensionless model, and that each dimensionless optimal parameter set we obtain corresponds to many possible "equivalent" dimensional parameter sets.

The methods used here should be regarded as a tool, to guide the design of a device that can be optimized for a choice of different effects. If a manufacturer is more concerned with switching at low fields, then our methods can be used to optimize the proposed device with a relatively large value of the weight ν; if higher surface energies are the primary concern, then small values of ν and γ should be chosen; while if good contrast is key, then a large value of μ should be used. In the examples presented here, the weights of the terms in the benefit function were chosen so as to give an approximate balance of all desired features, and with these weights contrast ratios of between 3.11 and 4.23 were obtained for the two steady states that form the basis of the device. Many other features that might be desirable in a device could, of course, similarly be incorporated into the benefit function using the approach described in this chapter: our benefit function is intended to be largely illustrative.

Of course, the proposed device is represented here by an idealized mathematical model, and we would not expect our results to be quantitatively correct in an experimental setup. Further work is needed to fine-tune the model. In particular, the assumptions that the electric field within the device is uniform, and that the two elastic constants K_1^* and K_3^* are equal, are not quantitatively correct. In Chapter 4 we present a more sophisticated model (steady-state in the first instance) in which

we solve for the electric field $\boldsymbol{E} = \nabla\phi$ within the sample, instead of assuming it to be uniform. While a time-dependent version of such a model can be formulated, a degree of quantitative uncertainty will persist since, while the gradient flow arguments of §2.1.2 can be extended to the new coupled Euler-Lagrange equations for the director angle θ and electric potential ϕ, the timescales of the relaxation of θ and ϕ will be different, and we do not know precisely how they will differ.

Another obvious question to ask is, how will variations parallel to the bounding surfaces affect device performance? Such variations could include gradients in surface energy (imparted by chemical treatments for instance, or UV irradiation); variable anchoring angle (similar treatments); variable surface topography (as is seen in the Zenithal Bistable Device (ZBD) [3] and Post-Aligned Bistable Device (PABD) [29]); or simply manufacturing nonuniformities. Addressing this question is the subject of Chapter 3.

CHAPTER 3

2D MODEL OF A BISTABLE DISPLAY DEVICE

3.1 Introduction and Motivation

In the investigation of the 1D model in which anchoring conditions (and hence solutions) are independent of x, it was found that at sufficiently weak anchoring strengths, bistability is possible, with two-way switching at moderate electric fields. The 1D model was optimized in the design parameter space of anchoring strengths and anchoring angles at the two surfaces, according to several criteria, principally: (i) maximize the anchoring strengths allowing two-way switching (to maximize device robustness); (ii) maximize the optical contrast between the two stable states. If specific weights are assigned to each of the criteria, an "optimal" device can be found, and examples of this are given in Chapter 2 (see also [9]). The optimization in that chapter was carried out in stages, the first stage being an optimization to maximize surface energies (i) and contrast (ii), for the case in which the anchoring angle $\alpha_1^{(0)}$ at the upper surface is related to $\alpha_0^{(0)}$ by $\alpha_1^{(0)} = \alpha_0^{(0)} - \pi/2$. (Since in this chapter we will be considering perturbations to this basic 1D model, we have introduced a zero superscript to denote the unperturbed 1D case.) Following this stage, the anchoring angle $\alpha_1^{(0)}$ is allowed to vary independently, and then further desirable criteria are introduced into the optimization.

As outlined at the end of Chapter 2 (§2.4), it is natural to consider how the results of the 1D investigation change when properties are allowed to vary in the plane of the device. Therefore, in this chapter we investigate the effect of adding 2D boundary perturbations to the 1D model. This study is motivated by several considerations: (i) it is likely that introducing spatial variation in the boundary will allow improvement on the 1D results, if done correctly; (ii) the 2D system is

mathematically more complex and will likely lead to bifurcations to new steady states and the possible disappearance of old ones; and (iii) in any real device boundary variations are inevitable (even if due only to edge effects) and a 2D study will shed some light on the robustness of the 1D results.

In the final optimal states achieved in the 1D simulations described in Chapter 2, the anchoring angle $\alpha_1^{(0)}$ is quite close to $\alpha_0^{(0)} - \pi/2$. Therefore, when using this 1D model as the basis for our 2D perturbations, we enforce this restriction, giving a smaller parameter space to consider. We also consider a fixed "switching protocol" when attempting to switch between the stable steady states: a transient electric field is applied at a fixed strength (characterized by $|\mathcal{F}| = 5$) for 25 dimensionless time units, and then decreased linearly to zero over a further 5 dimensionless time units (corresponding to a total dimensional switching time of perhaps 150 ms). With these restrictions, the entire region of $(\mathcal{A}_0, \mathcal{A}_1, \alpha_0^{(0)})$-space in which bistability with two-way switching is achieved in the 1D model may be mapped out with reasonable computational effort. This region is shown in Figure 3.1. For triplets $(\mathcal{A}_0, \mathcal{A}_1, \alpha_0^{(0)})$ outside this region, no two-way switching is found in the 1D model.

3.2 Mathematical Model

The basic setup is a layer of nematic liquid crystal (NLC), sandwiched between parallel bounding surfaces at $z^* = 0$ and $z^* = h^*$. Star superscripts will be used throughout to denote dimensional quantities, and will be dropped when we nondimensionalize. The molecules of the NLC are rod-like, which imparts anisotropy. The molecules like to align locally, which is modeled by associating an elastic energy with any deviations from uniform alignment (§3.2.1 below). The local average molecular orientation is described by a director field $\boldsymbol{n}$, a unit vector which, in our 2D model, is confined to the (x^*, z^*)-plane, see Figure 2.1. It may, therefore, be expressed in terms of a single

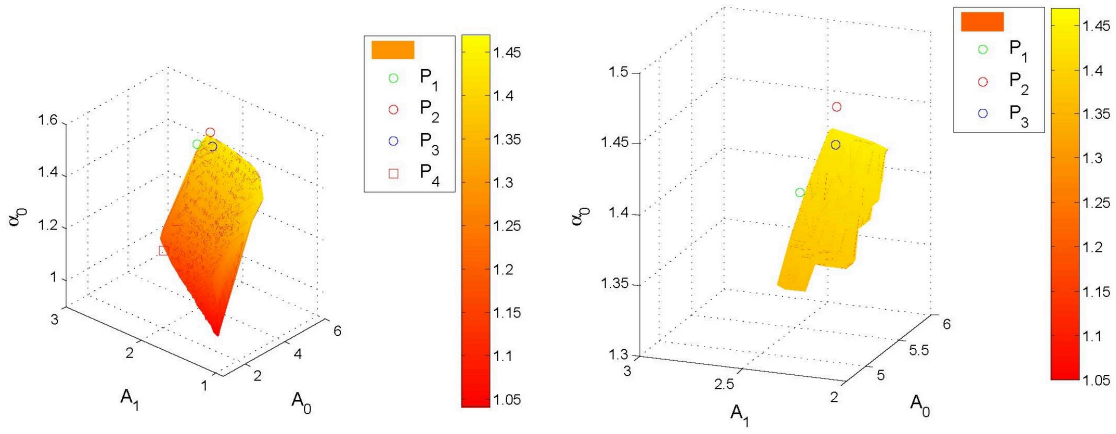

Figure 3.1 Left: the region of $(\mathcal{A}_0, \mathcal{A}_1, \alpha_0^{(0)})$ parameter space within which two-way switching is achieved for the 1D model. The points P_1, P_2, P_3, P_4 refer to test points with respect to which we perturb, and are discussed in detail in the text. Right: A zoom of the region around P_1, P_2, P_3. Colorbar displays the level of corresponding α_0-value of points.

angle $\theta(x^*, z^*, t^*)$,

$$\boldsymbol{n} = (\sin\theta, 0, \cos\theta), \tag{3.1}$$

where t^* is time. We further assume that the electric field, when applied, is uniform throughout the NLC layer: $\boldsymbol{E}^* = E^*(t^*)(0, 0, 1)$. In reality the electric field and the NLC interact, so that even if $\boldsymbol{E}^*$ is uniform outside the layer, it will vary across the layer. This issue will be addressed in Chapter 4; however, we do not expect such variation to be significant, and we expect the uniform field assumption is sufficient for the proof-of-principle investigation here. We recall that in any case, an electric field is utilized only to switch the nematic configuration from one state to the other, and therefore the detailed properties of the field are not so important.

Since we require bistability in the absence of an applied field, anchoring conditions at the bounding surfaces $z^* = 0, h^*$ are key. The anchoring pretilt angle (denoted by α in our model, the preferred value of θ at either interface) may be controlled by a variety of surface treatments; for example, mechanical or chemical

treatments, nano-patterning, and surface irradiation, have all been shown to produce certain desired anchoring angles and strengths, as discussed in the Introduction. We shall therefore assume that surface anchoring angles and strengths are adjustable parameters, within a range of physically-realistic values. We shall furthermore allow the anchoring angles to vary sinusoidally about some average value:

$$\alpha_i = \alpha_i^{(0)} + \delta_i \cos(2\pi x^*/L^* + \phi_i) \qquad i = 0, 1, \tag{3.2}$$
$$\phi_0 = 0,\ \phi_1 \in [0, \pi/2]$$

where $i = 0, 1$ denotes the lower/upper bounding surface, respectively, and $\phi_1 \neq 0$ allows for a phase difference between the variations on each surface. We expect that such periodic variation will approximate the situation in which the bounding surfaces themselves have periodically-varying topography (possibly with a phase difference between upper and lower surfaces) as seen, for example, in the Zenithal Bistable Device (ZBD) or Post Aligned Bistable Device (PABD) [3,29]. We consider two cases for the amplitude parameters δ_0, δ_1: (i) they take the same value, $\delta_1 = \delta_0 = \delta$, or (ii) $\delta_1 = 0$, $\delta_0 = \delta$ (perturbation only on the lower boundary).

3.2.1 Energetics

The free energy of the liquid crystal layer, in the presence of an applied electric field and with specified anchoring conditions at each bounding surface, has several contributions. The bulk free energy density consists of elastic, dielectric and flexoelectric contributions W_e^*, W_d^*, W_f^*, and in our 2D model with the uniform field assumption these are given by

$$2W_e^* = K_1^*(\nabla^* \cdot \boldsymbol{n})^2 + K_3^*((\nabla^* \times \boldsymbol{n}) \times \boldsymbol{n})^2,$$
$$2W_d^* = -\varepsilon_0^*(\varepsilon_\parallel - \varepsilon_\perp)(\boldsymbol{n} \cdot \boldsymbol{E}^*)^2,$$
$$W_f^* = -\boldsymbol{E}^* \cdot (e_1^*(\nabla^* \cdot \boldsymbol{n})\boldsymbol{n} + e_3^*(\nabla^* \times \boldsymbol{n}) \times \boldsymbol{n}),$$

where K_1^* and K_3^* are elastic constants, ε_0^* is the permittivity of free space, $\varepsilon_\parallel$ and $\varepsilon_\perp$ are the relative dielectric permittivities parallel and perpendicular to the long axis of the nematic molecules, and e_1^* and e_3^* are flexoelectric constants [4, 12, 27]. With the director field $\boldsymbol{n}$ as given by (3.1), and the common simplifying assumption $K_1^* = K_3^* = K^*$, the total bulk free energy density $W^* = W_e^* + W_d^* + W_f^*$ simplifies. Introducing the nondimensional forms $W = K^* W^*/h^{*2}$ and $(x, z) = (x^*, z^*)/h^*$,

$$W = \frac{1}{2}(\theta_x^2 + \theta_z^2) - \mathcal{D}\cos^2\theta + \frac{\mathcal{F}}{2}(\theta_z \sin 2\theta - \theta_x \cos 2\theta) \tag{3.3}$$

where

$$\mathcal{D} = \frac{h^{*2}E^{*2}\varepsilon_0^*(\varepsilon_\parallel - \varepsilon_\perp)}{2K^*}, \quad \mathcal{F} = \frac{h^* E^*(e_1^* + e_3^*)}{K^*} \tag{3.4}$$

are dimensionless constants. With representative characteristic values $h^* \sim 2\mu$m, $E^* \sim 1\text{V}\mu\text{m}^{-1}$, $e_1^* + e_3^* \sim 5 \times 10^{-11}\text{C m}^{-1}$, $K^* \sim 1 \times 10^{-11}$N, $\varepsilon_\parallel - \varepsilon_\perp \sim 5$ [2, 11, 22], both $\mathcal{D}$ and $\mathcal{F}$ are $O(1)$. We emphasize that these values are *not* intended to be absolute; a fair degree of variation about these values is possible, and indeed, many different combinations of dimensional parameter values will lead to the same model in dimensionless form. Note that $\mathcal{D}$ and $\mathcal{F}$ are not independent; the ratio

$$\Upsilon = \frac{\mathcal{F}^2}{\mathcal{D}} = \frac{2(e_1^* + e_3^*)^2}{K^*\varepsilon_0^*(\varepsilon_\parallel - \varepsilon_\perp)} \tag{3.5}$$

is a material parameter, independent of the geometry. We consider the most common case in which the dielectric anisotropy $\varepsilon_\parallel - \varepsilon_\perp > 0$ (molecules align parallel, rather than perpendicular, to an applied field), so that $\mathcal{D} > 0$ always. The parameter $\mathcal{F}$ characterizing the dimensionless strength of the applied electric field will, however, change sign if the electric field direction is reversed. Since the representative parameter values listed above give $\Upsilon \approx 10$, we assign this value to Υ throughout our computations.

The surface anchoring is modeled by a Rapini-Papoular form [23]; if $g^*_{\{0,h^*\}} = (K^*/h^*)g_{\{0,1\}}$ are the surface energies per unit length at the boundaries $z^* = 0,\, h^*$, then

$$g_{0,1} = \frac{\mathcal{A}_{\{0,1\}}}{2}\sin^2(\theta - \alpha_{\{0,1\}}), \quad \mathcal{A}_{\{0,1\}} = \frac{h^* A^*_{\{0,h^*\}}}{K^*} \tag{3.6}$$

where $A^*_{\{0,h^*\}}$ are the anchoring strengths at $z^* = 0,\, h^*$ and $\alpha_{\{0,1\}}$ are the preferred angles, given by (3.2): in dimensionless form,

$$\alpha_i = \alpha_i^{(0)} + \delta_i \cos(2\pi x/L + \phi_i) \qquad i = 0, 1, \tag{3.7}$$
$$\phi_0 = 0,\, \phi_1 \in [0, \pi/2]$$

where the dimensionless perturbation wavelength $L = L^*/h^*$. Figure 2.1 summarizes the setup and notation.

The total (dimensionless) free energy for the system is given by

$$J = \int_0^1 \int_0^L W(\theta, \theta_z)\, dxdz + \int_0^L g_0(x)|_{z=0}\, dx + \int_0^L g_1(x)|_{z=1}\, dx,$$

and equilibrium solutions are those functions $\theta(x, z)$ that minimize J. The standard calculus of variations approach, with $\theta(x, z) \mapsto \theta(x, z) + \epsilon\eta(x, z)$ $(0 < \epsilon \ll 1)$ leads to $J \mapsto J[\theta + \epsilon\eta] = J_0 + \epsilon J_1 + \epsilon^2 J_2 + O(\epsilon^3)$, and for θ to be a minimizer of J, we require $J_1 = 0,\, J_2 > 0$, for all admissible variations η (the condition on J_2 ensures we have a minimum, rather than a maximum, of the free energy). After Taylor expansion and integration by parts, we have

$$J_1 = \int_0^1 \int_0^L \eta \left(W_\theta - \left(W_{\theta_z}\right)_z - \left(W_{\theta_x}\right)_x\right) dxdz + \int_0^L \eta(g_{0\theta} - W_{\theta_z})|_{z=0}\, dx + \int_0^L \eta(g_{1\theta} + W_{\theta_z})|_{z=1}\, dx - \int_0^1 \eta W_{\theta_x}|_{x=0}\, dz + \int_0^1 \eta W_{\theta_x}|_{x=L}\, dz.$$

The condition that this vanishes for all admissible variations η leads to the usual Euler-Lagrange equation for θ, subject to boundary conditions on $z = 0$, 1:

$$W_\theta - \left(W_{\theta_x}\right)_x - \left(W_{\theta_z}\right)_z = 0, \tag{3.8}$$

$$(g_{0\theta} - W_{\theta_z})|_{z=0} = 0, \quad (g_{1\theta} + W_{\theta_z})|_{z=1} = 0. \tag{3.9}$$

The net contribution to J_1 coming from $x = 0$, 1 is easily seen to vanish for the form of W specified by (3.3) if periodic boundary conditions on θ are enforced (both θ and θ_x continuous). We note that the second variation J_2 may be easily calculated if required to check stability. However, in practice we find all steady states by solving a diffusive equation arising from a gradient flow model (below), which guarantees that only stable steady states are found.

3.2.2 Time-dependent Energetics: Gradient Flow

As discussed in Chapter 2 for the 1D case, if the system is not initially at equilibrium then it will evolve over time towards a steady state described by the above equations. An accurate description of these dynamics requires the full equations of nematodynamics [12, 20], which couple flow to director reorientation. For our explorations of parameter space that follow, however, the full model is extremely computationally intensive and instead we follow several other authors (e.g., Kedney & Leslie [15] and Davidson & Mottram [11]) in assuming that the system evolves in the direction that minimizes its total free energy (a gradient flow). Both bulk and surface components will evolve in this way, and this process leads to

$$\theta_t + W_\theta - \left(W_{\theta_x}\right)_x - \left(W_{\theta_z}\right)_z = 0,$$

$$(\tilde{\nu}\theta_t + g_{0\theta} - W_{\theta_z})|_{z=0} = 0, \quad (\tilde{\nu}\theta_t + g_{1\theta} + W_{\theta_z})|_{z=1} = 0,$$

with the choice of dimensionless time set by

$$t = t^* \frac{K^*}{\tilde{\mu}^* h^{*2}} \tag{3.10}$$

where $\tilde{\mu}^*$ is the dimensional rotational viscosity of the NLC molecules, typically around 0.1 N s m^{-2}). With bulk and surface energy densities given by (3.3) and (3.6), the system becomes

$$\theta_t = \theta_{xx} + \theta_{zz} - \mathcal{D} \sin 2\theta \tag{3.11}$$

$$\tilde{\nu}\theta_t = \theta_z - \frac{\mathcal{A}_0}{2} \sin 2(\theta - \alpha_0) + \frac{\mathcal{F}}{2} \sin 2\theta \text{ on } z = 0 \tag{3.12}$$

$$-\tilde{\nu}\theta_t = \theta_z + \frac{\mathcal{A}_1}{2} \sin 2(\theta - \alpha_1) + \frac{\mathcal{F}}{2} \sin 2\theta \text{ on } z = 1 \tag{3.13}$$

with $\mathcal{D}$ (dimensionless dielectric coefficient), $\mathcal{F}$ (dimensionless field strength), $\mathcal{A}_{\{0,1\}}$ (dimensionless surface energy) and $\alpha_{\{0,1\}}$ (anchoring angles) given by (3.4), (3.6) and (3.7). An initial condition $\theta(x, z, 0)$ closes the model. When θ is independent of time, (3.11)–(3.13) are exactly the steady-state model, specified by (3.8), (3.9). We will investigate the multistability and switching of (3.11)–(3.13) as the anchoring angle perturbation parameters δ, L, ϕ are varied. Before doing so, we first remind the reader of the relevant results of Chapter 2 for the analogous 1D model.

3.2.3 Summary of Key Results of the 1D Model

In the investigation of the 1D model in which anchoring conditions (and hence solutions) are independent of x, it was found that at sufficiently weak anchoring strengths, bistability is possible, with two-way switching at moderate electric fields. The 1D model was optimized in the parameter space defined by parameters that may be varied in experiments – anchoring strengths and anchoring angles at the two surfaces. The optimization was carried out according to several criteria, principally: (i) maximize the anchoring strengths allowing two-way switching (to maximize robustness); (ii) maximize the optical contrast between the two stable states. If specific weights

are assigned to each of the criteria, an "optimal" configuration can be found, and examples of this optimization are given in Chapter 2. The optimization in that chapter was carried out in stages, the first stage being an optimization to maximize surface energies (i) and contrast (ii), for the case in which the anchoring angle $\alpha_1^{(0)}$ at the upper surface is related to $\alpha_0^{(0)}$ by

$$\alpha_1^{(0)} = \alpha_0^{(0)} - \pi/2. \tag{3.14}$$

Following this stage the anchoring angle $\alpha_1^{(0)}$ is allowed to vary independently, and then further desirable criteria are introduced into the optimization.

In the final optimal states achieved in those trials, the anchoring angle $\alpha_1^{(0)}$ is quite close to $\alpha_0^{(0)} - \pi/2$. Therefore, when using this 1D model as the basis for the 2D geometry considered in the present work, we enforce the restriction given by (3.14), giving a smaller parameter space to consider. We also consider a fixed "switching protocol" when attempting to switch between the stable steady states: a transient electric field is applied at a fixed strength (characterized by $|\mathcal{F}| = 5$) for 20 dimensionless time units, and then decreased linearly to zero over a further 5 dimensionless time units (corresponding to a total dimensional switching time of about 150 ms).

With these restrictions, the entire region of $(\mathcal{A}_0, \mathcal{A}_1, \alpha_0^{(0)})$-space in which bistability with two-way switching is achieved in the 1D model may be mapped out with reasonable computational effort. Figure 3.1 shows this region. For triplets $(\mathcal{A}_0, \mathcal{A}_1, \alpha_0^{(0)})$ outside this region, no two-way switching is found in the 1D model. Note in particular the existence of definitive upper bounds on the anchoring strengths $\mathcal{A}_0$, $\mathcal{A}_1$, at which the two-way switching is obtained.

3.3 The 2D Model Investigations

Our aim is to investigate the effect of adding 2D boundary perturbations to the 1D model. This study is motivated by several considerations: (i) it is likely that introducing spatial variation in the boundary will allow the region where two-way switching occurs to be extended; (ii) the 2D system is mathematically more complex and will likely lead to bifurcations to new steady states and the possible disappearance of old ones; and (iii) in any real device boundary variations are inevitable (even if due only to edge effects) and a 2D study will shed some light on the robustness of the 1D results.

We perturb the 1D model by replacing the constant anchoring angles $\alpha_0^{(0)}$, $\alpha_1^{(0)}$ at the boundaries by sinusoidally-varying angles given by (3.7) (with $\alpha_1^{(0)} = \alpha_0^{(0)} - \pi/2$). As noted earlier, we may view such a perturbation as due either to surface treatment, which alters the surface chemistry and causes the anchoring angle to vary; or as an approximation to the changes in anchoring caused by topographical variation in the bounding surfaces (as in the ZBD or PABD devices [3, 29]). One motivation is to increase the size of the region where two-way switching is possible (relative to that for the 1D model), and a key consideration is increasing the anchoring strengths at which two-way switching can be obtained. Hence, we first consider how this might be achieved.

We choose points $(\mathcal{A}_0, \mathcal{A}_1, \alpha_0^{(0)})$ in our parameter space that are *outside* the two-way switching region illustrated in Figure 3.1, but close to its boundary. In particular, we increase the surface energies beyond the confines of the 1D switching region. For such points, two-way switching is not achievable within the 1D framework; but in 2D it may be possible. We choose three such points to investigate, all in the region of parameter space close to the highest allowable surface energies: points $P_1 = (5.41, 2.45, 1.40)$, $P_2 = (5.50, 2.30, 1.46)$ and $P_3 = (4.85, 2.10, 1.46)$. Other points (including some that are far from the 1D optimum) were investigated, but

did not yield significantly different results from those for these three points. We summarize results also for one such point, P_4, that is far from optimal in the 1D model.

For each chosen point, we perturb the anchoring boundary conditions in several ways. (i) Perturb the anchoring only at the lower boundary. This involves setting $\delta_1 = 0$ in (3.7) and, with no loss of generality, $\phi_0 = 0$, leaving just two perturbation parameters δ and L. (ii) Perturb the anchoring at both boundaries, with the same amplitude $\delta_1 = \delta_0 = \delta$, and with no phase difference between the boundaries: $\phi_0 = 0$, leaving just two perturbation parameters δ and L. (iii) Perturb the anchoring at both boundaries, with the same amplitude $\delta_1 = \delta_0 = \delta$, and with variable phase difference between the boundaries: $\phi_0 = \phi \in [0, \pi/2]$, but fixing the domain length L. This again leaves just two perturbation parameters, δ and ϕ.

We describe the outcome of these investigations below. In all cases we use numerical continuation to generate our basic stable states. We start from the 1D problem, where the two stable steady states, which we label $\boldsymbol{n}_1$ and $\boldsymbol{n}_2$, are known analytically in (2.16), (2.17). We then apply a small perturbation, $\delta = 0.1$, using each 1D steady state as an initial condition in (3.11)–(3.13) (at zero field, $\mathcal{D} = \mathcal{F} = 0$). We solve these equations using a standard ADI scheme, and look for steady-state solutions, which are in practice found by evolving (3.11)–(3.13) until the results do not change further (typically it is enough to simulate until $t = 30$ (dimensionless time units) to ensure that true steady-state solutions are found). Then, we use these newly found steady-state solutions as initial conditions for the more strongly perturbed case, with $\delta = 0.2$, and so on. If at any stage a new steady state appears, backward continuation in δ is used to locate its first appearance. We then subject all solutions found to our switching protocol (apply a transient electric field, as for the 1D case described in §3.2.3 above). It is possible that this produces new steady states.

If this happens, these states are also tracked using continuation in δ, as described above.

To illustrate further the coexistence of the multiple steady states and the transitions between them, we also construct bifurcation diagrams in several cases, by plotting a norm of the (stable) steady states versus δ:

$$\text{norm}(\boldsymbol{n}) := \sqrt{\sum_{i,j=1}^{M,N} \left(\frac{\theta_{i,j}(\text{mod}.\pi)^2)}{MN} \right)}, \tag{3.15}$$

where $\theta_{i,j}$ is the discretization of the director angle θ at grid point (i, j), and M, N are the total number of mesh grid points in each direction. The different steady states have different norms, hence the solution branches are distinct when plotted in this way and bifurcations are evident. Since (as described above) all steady states are found by time-evolving the dynamic system until no further change is seen, this method of constructing the bifurcation diagram can produce only the stable solution branches. No unstable steady solutions are found by our methods.

3.4 Results

We summarize our results for each type of boundary perturbation, and for each of the three chosen "test points" in parameter space, below. The system exhibits rich behavior, with as many as four distinct steady states found in certain parameter regimes. We label these four steady states $\boldsymbol{n}_1$, $\boldsymbol{n}_2$, $\boldsymbol{n}_3$, $\boldsymbol{n}_4$. In accordance with our continuation methods, $\boldsymbol{n}_1$ and $\boldsymbol{n}_2$ are always the continuations of the 1D steady states found in the unperturbed problem (consistent with the results of Chapter 2), while $\boldsymbol{n}_3$ and $\boldsymbol{n}_4$ are new states that only exist with perturbed anchoring. The results on switching are presented symbolically to denote the outcome at each point in parameter space, with reference to the global legend presented in Figure 3.2. Each symbol in

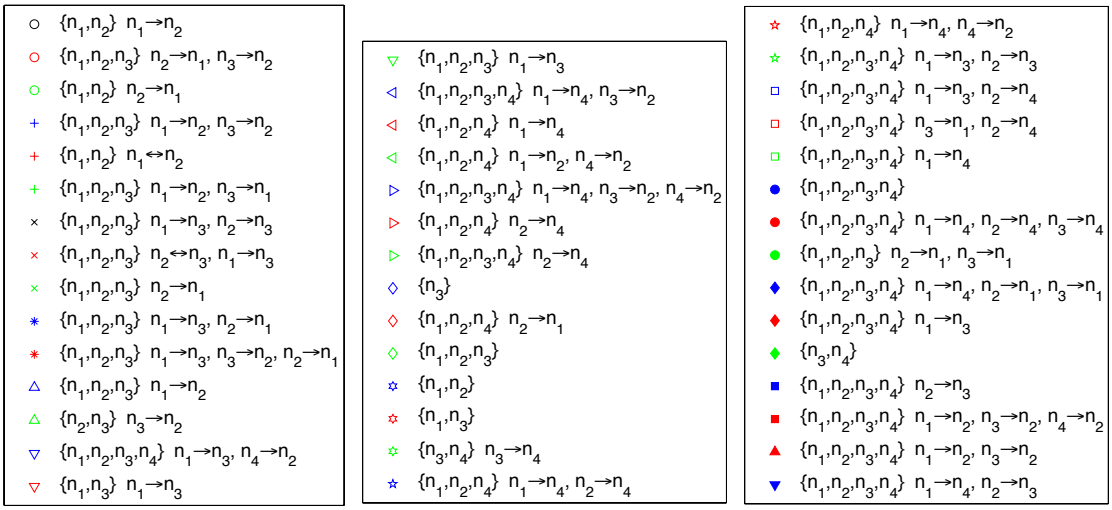

Figure 3.2 Explanation of symbols used in the switching results that follow below. The notation within braces denotes which steady states exist at a given point in parameter space. The statement $\mathrm{n_i} \to \mathrm{n_j}$ denotes that switching occurs from state $\boldsymbol{n}_i$ to $\boldsymbol{n}_j$; and $\mathrm{n_i} \leftrightarrow \mathrm{n_j}$ denotes that two-way switching occurs between states $\boldsymbol{n}_i$ and $\boldsymbol{n}_j$.

that legend records which steady states exist (listed within braces $\{\cdot\}$), and what switching is found between those states (denoted by directional arrows as described in the caption). An example of three coexisting steady states is shown in Figure 3.3.

We note that exploring the complete 3D parameter space shown in Figure 3.1 would be computationally very demanding. The discussion that follows is limited to illustrating just some features of the results that may be expected.

3.4.1 Equal-amplitude Perturbations with Zero Phase Difference

Here we consider the domain with anchoring angles α_0, α_1 at lower and upper boundaries given by

$$\begin{aligned} \alpha_0 &= \alpha_0^{(0)} + \delta\cos(2\pi x/L), \\ \alpha_1 &= \alpha_0^{(0)} - \pi/2 + \delta\cos(2\pi x/L), \end{aligned} \tag{3.16}$$

as the perturbation amplitude δ and domain length L vary.

3.4.1.1 Point P_1, $(\mathcal{A}_0, \mathcal{A}_1, \alpha_0^{(0)}) = (5.41, 2.45, 1.40)$.

Figure 3.4 shows the results of the switching investigation when the 1D case represented by point P_1 in $(\mathcal{A}_0, \mathcal{A}_1, \alpha^{(0)})$-space is perturbed at both boundaries, with no phase difference, as in (3.16). We see that for sufficiently small perturbation amplitude δ, the continuations of the two 1D stable steady states exist, and there is still no two-way switching between them. This is to be anticipated, since the point P_1 lies outside the switching region for the 1D problem. As δ increases however, more complex behavior emerges.

For sufficiently small values of L, once δ passes a first threshold value, a window of two-way switching $\boldsymbol{n}_1 \leftrightarrow \boldsymbol{n}_2$ is observed. This is already a significant finding, since it shows that two-way switching is possible in the 2D geometry even if it does not occur for the 1D case. This window disappears when δ passes a second threshold value. Both threshold values decrease as L increases. When δ is increased further still, a new steady state $\boldsymbol{n}_3$ is observed. As an illustration, Figure 3.3 shows $\boldsymbol{n}_1$, $\boldsymbol{n}_2$, $\boldsymbol{n}_3$ as vector plots in (x, z)-space over a single wavelength, for $(L, \delta) = (4, 0.7)$.

For small values of L, $\boldsymbol{n}_3$ appears to arise from a pitchfork bifurcation of $\boldsymbol{n}_1$ and $\boldsymbol{n}_2$, as shown in Figure 3.5. This figure shows a bifurcation diagram, constructed by plotting a norm of the (stable) steady states versus δ (see (3.15)). Figure 3.5 shows bifurcation diagrams for the cases $L = 0.5$ and $L = 4$: the case $L = 0.5$ clearly indicates the pitchfork bifurcation. For this value of L the stable steady state $\boldsymbol{n}_3$ never coexists with stable steady states $\boldsymbol{n}_1$ and $\boldsymbol{n}_2$, but replaces them at large δ. As described in §3.3, these bifurcation diagrams show only the stable solution branches; unstable steady solutions are not found by our methods.

Figure 3.4 shows that for larger values of L, $L \gtrsim 2$, the two-way switching between $\boldsymbol{n}_1$ and $\boldsymbol{n}_2$ is suppressed. The stable steady state $\boldsymbol{n}_3$ appears sooner, at smaller values of δ, and now coexists with $\boldsymbol{n}_1$ and $\boldsymbol{n}_2$. For $L = 3$, although there is no two-way switching $\boldsymbol{n}_1 \leftrightarrow \boldsymbol{n}_2$, we do find two-way switching between $\boldsymbol{n}_2$ and $\boldsymbol{n}_3$ (for

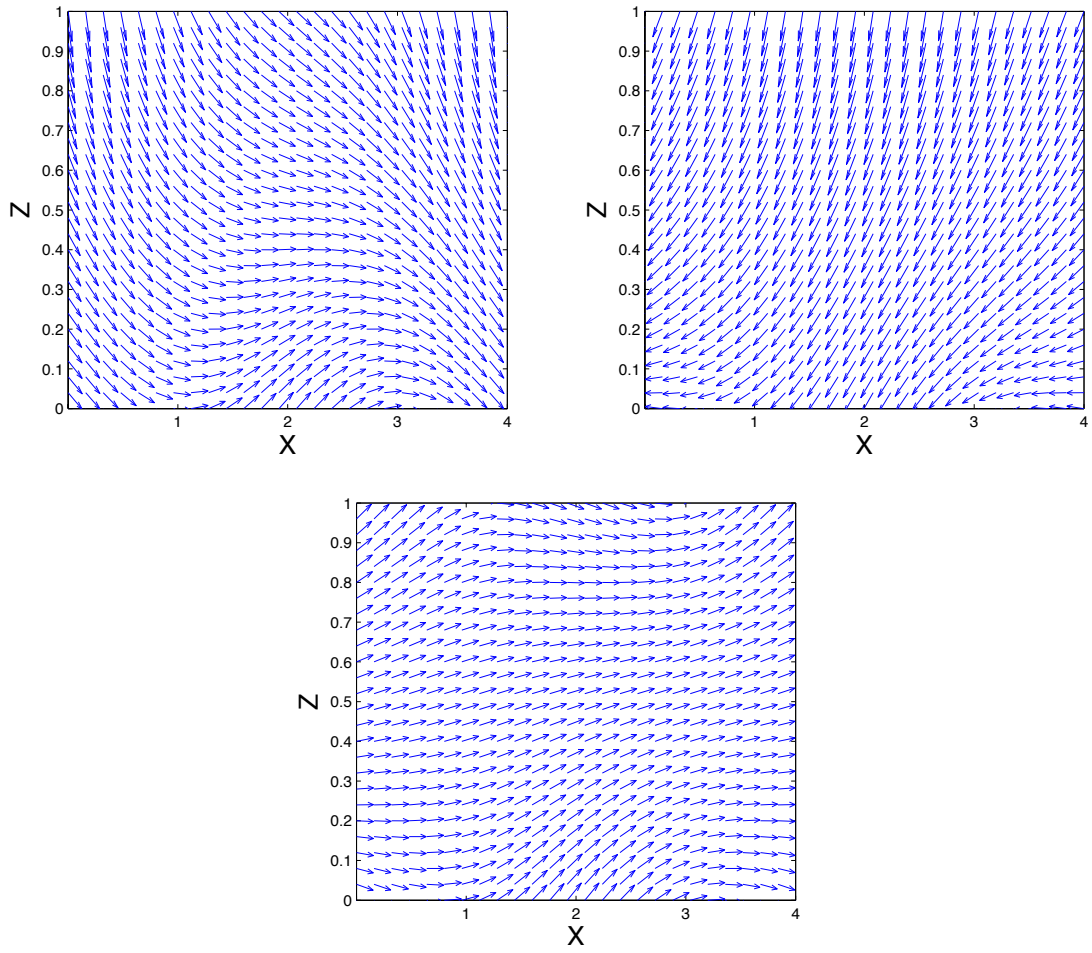

Figure 3.3 The three steady states $\boldsymbol{n}_1$, $\boldsymbol{n}_2$, $\boldsymbol{n}_3$, corresponding to the point $(L, \delta) = (4, 0.7)$ in Figure 3.4.

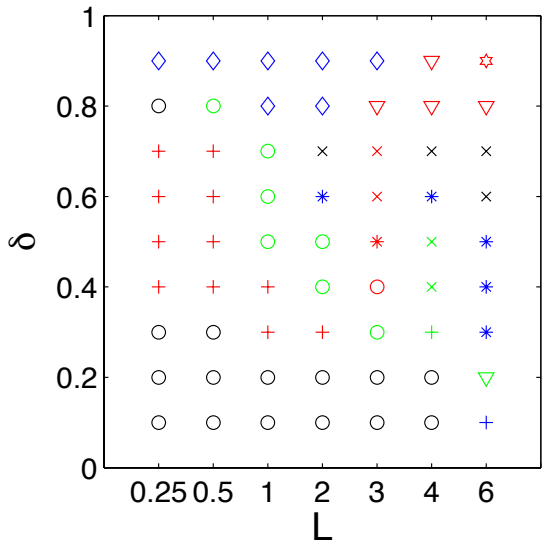

Figure 3.4 Switching results when perturbing the 1D case represented by point P_1, $(\mathcal{A}_0, \mathcal{A}_1, \alpha_0^{(0)}) = (5.41, 2.45, 1.40)$, according to (3.16). Symbols are defined in the global legend of Figure 3.2.

$\delta = 0.6, 0.7$, and presumably also in some surrounding neighborhood of (L, δ)-space), and for $\delta = 0.5$ it is particularly interesting to observe *cyclic* switching involving all three steady states: we see the switching sequence $\boldsymbol{n}_1 \to \boldsymbol{n}_3 \to \boldsymbol{n}_2 \to \boldsymbol{n}_1$. We expect that this cyclic switching occurs in some small surrounding neighborhood of (L, δ)-space.

For $L = 6$ (the largest value of L considered) the steady state $\boldsymbol{n}_3$ appears even for the smallest value of δ used, $\delta = 0.1$. More generally, though more steady states exist with (one would imagine) greater potential for switchability for larger L, no two-way switching is found for $L > 3$. Another consequence of longer domains (larger L) is an increased degree of solution complexity, as is apparent from the bifurcation diagram shown in Figure 3.5(b).

The steady state $\boldsymbol{n}_3$, once formed, appears rather robust under the conditions investigated here: other than the switching noted above for $L = 3$, and $\boldsymbol{n}_3 \to \boldsymbol{n}_2$ switching at small δ for $L = 6$, no switching was found from this state to any other. Far more switching is found from the steady states $\boldsymbol{n}_1$ and $\boldsymbol{n}_2$ to other states.

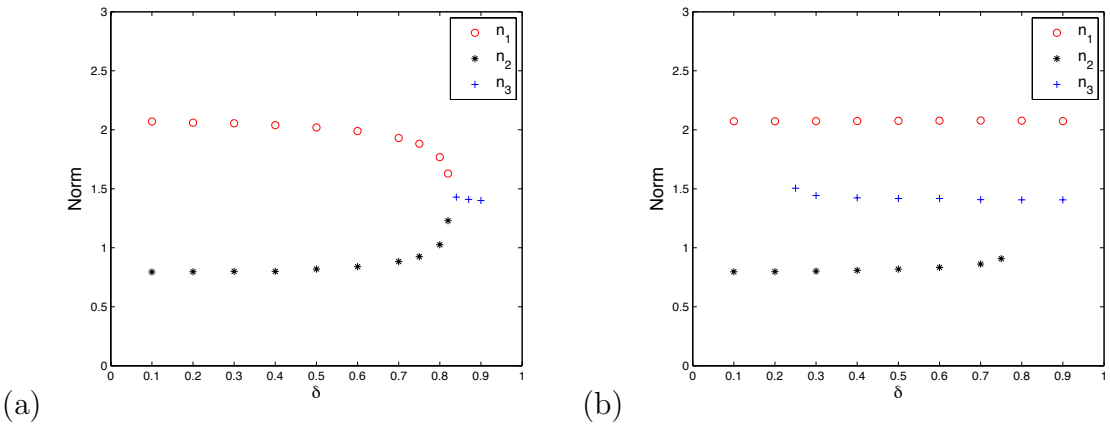

(a) (b)

Figure 3.5 Bifurcation diagrams representing stable steady states obtained when perturbing the 1D case represented by point P_1, $(\mathcal{A}_0, \mathcal{A}_1, \alpha_0^{(0)}) = (5.41, 2.45, 1.40)$, for the cases $L = 0.5$ (a) and $L = 4$ (b).

3.4.1.2 Point P_2, $(\mathcal{A}_0, \mathcal{A}_1, \alpha_0^{(0)}) = (5.50, 2.30, 1.46)$.

Figure 3.6 shows results when the 1D case represented by point P_2 in $(\mathcal{A}_0, \mathcal{A}_1, \alpha^{(0)})$ is perturbed at both boundaries, with no phase difference, as in (3.16). For very short domains, no two-way switching is found, at any perturbation amplitude. Only the two steady states $\boldsymbol{n}_1$ and $\boldsymbol{n}_2$ exist until $\delta = 0.9$, when the third steady state $\boldsymbol{n}_3$ appears. This state replaces both $\boldsymbol{n}_1$ and $\boldsymbol{n}_2$; see also the bifurcation plot in Figure 3.7(a). As the length L is increased slightly (as with the point P_1) a window of two-way switching opens for a range of δ-values. Again, at higher δ the third steady state $\boldsymbol{n}_3$ appears, and the δ-value at which $\boldsymbol{n}_3$ appears decreases as L increases. At $L = 2$ yet another steady state $\boldsymbol{n}_4$ appears at large δ: at this L-value as δ increases we have just two steady states for $0 \leq \delta \leq 0.5$, with two-way switching for $\delta = 0.3, 0.4$; for $\delta = 0.6, 0.7$ three steady states $\boldsymbol{n}_1$, $\boldsymbol{n}_2$, $\boldsymbol{n}_3$ coexist; for $\delta = 0.8$ just $\boldsymbol{n}_3$ exists; and for $\delta = 0.9$ the new steady state $\boldsymbol{n}_4$ comes into existence, coexisting with $\boldsymbol{n}_3$. No further two-way switching is found, however. For larger values $L > 3$, though the solution space becomes much richer and more complex, no two-way switching is found between any pair of stable states, even though for some parameter ranges all four steady states can coexist (see the bifurcation diagram for $L = 4$ in Figure

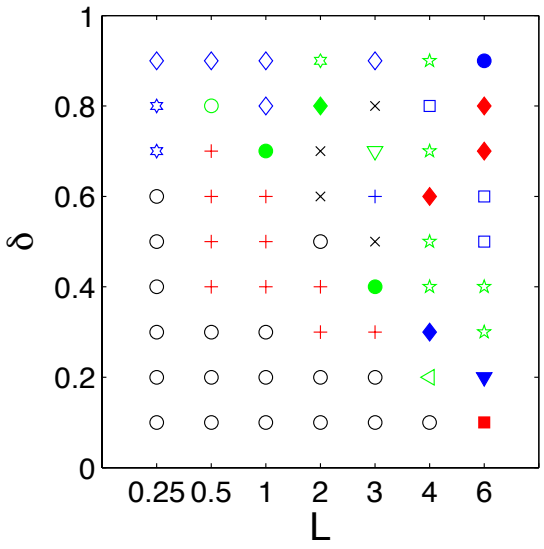

Figure 3.6 Switching results when perturbing the 1D case represented by point P_2, $(\mathcal{A}_0, \mathcal{A}_1, \alpha_0^{(0)}) = (5.50, 2.30, 1.46)$, according to (3.16).

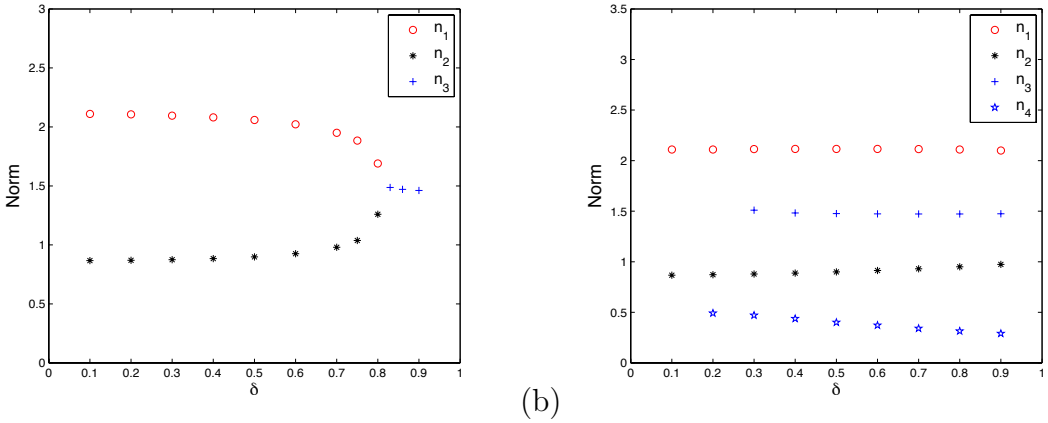

(a) (b)

Figure 3.7 Bifurcation diagrams representing stable steady states obtained when perturbing the 1D case represented by point P_2, $(\mathcal{A}_0, \mathcal{A}_1, \alpha_0^{(0)}) = (5.50, 2.30, 1.46)$, for the cases $L = 0.5$ (a) and $L = 4$ (b).

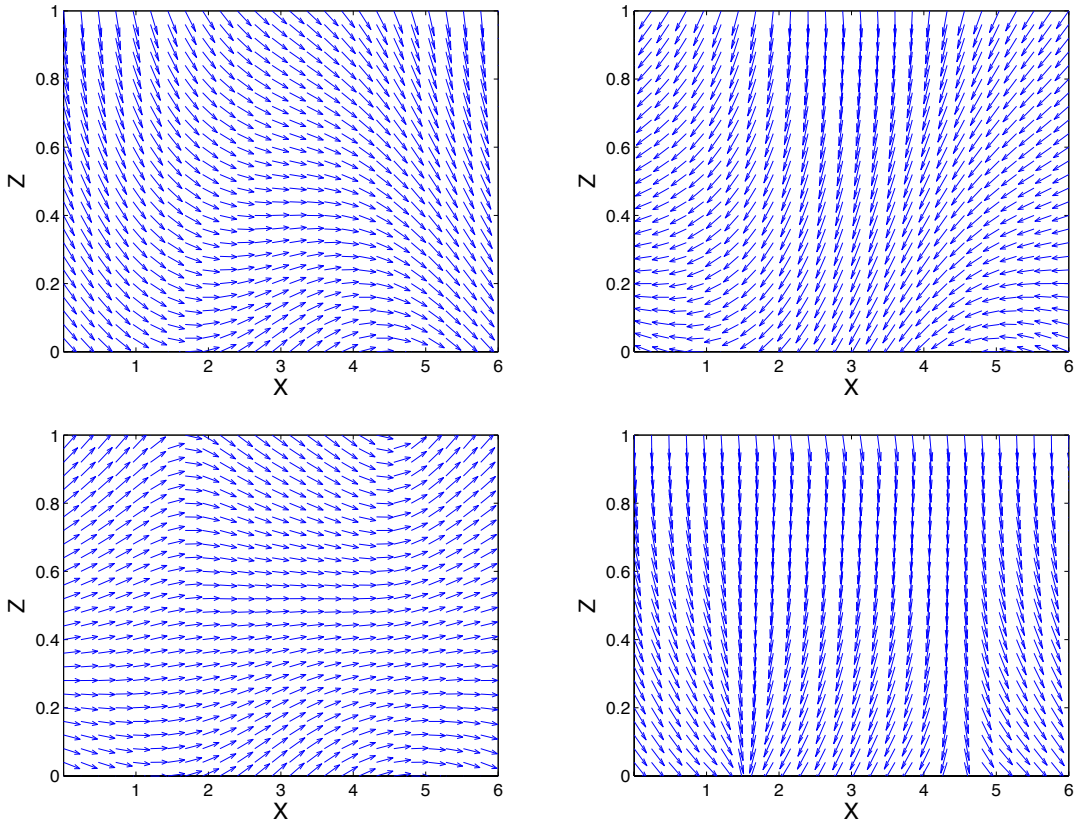

Figure 3.8 The four steady states $\boldsymbol{n}_1$, $\boldsymbol{n}_2$, $\boldsymbol{n}_3$, $\boldsymbol{n}_4$, corresponding to the point $(L, \delta) = (6, 0.6)$ in Figure 3.6.

3.7(b) where the four states coexist for a wide range of δ values). The steady state $\boldsymbol{n}_4$ appears to be particularly stable here, since it does not switch to any other state.

The trend of two-way switching for smaller domains, and of increased solution complexity for longer domains, is as seen for the point P_1 described above. Increased complexity could be loosely explained based on the increased ability of the director orientation to find additional configurations; however, we do not have a good explanation for the lack of two-way switching for these large domains.

Examples of the four steady states that can coexist are shown in Figure 3.8.

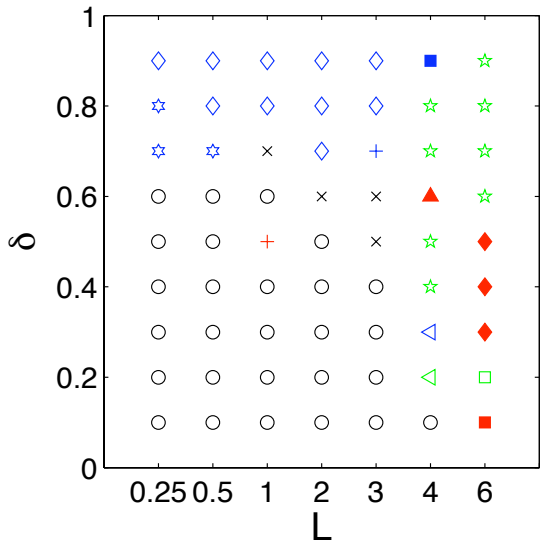

Figure 3.9 Switching results when perturbing the 1D case represented by point P_3, $(\mathcal{A}_0, \mathcal{A}_1, \alpha_0^{(0)}) = (4.85, 2.10, 1.46)$, according to (3.16).

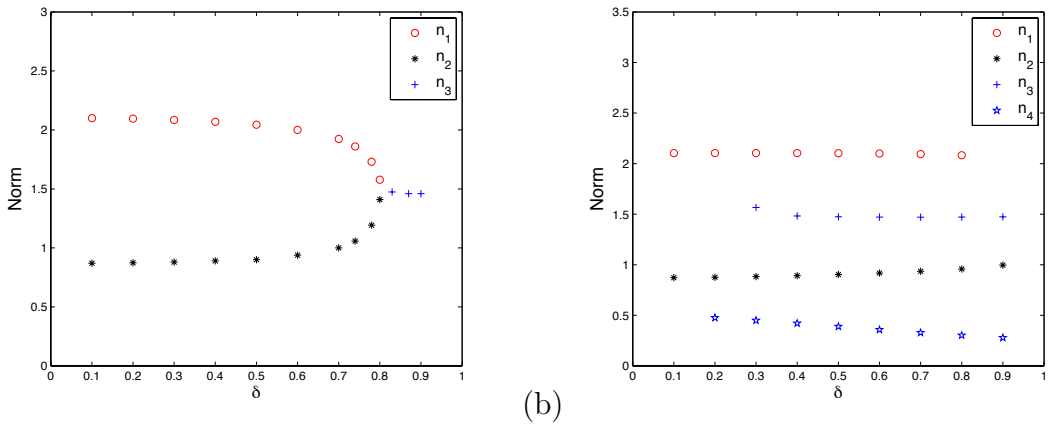

(a) (b)

Figure 3.10 Bifurcation diagrams representing stable steady states obtained when perturbing the 1D case represented by point P_3, $(\mathcal{A}_0, \mathcal{A}_1, \alpha_0^{(0)}) = (4.85, 2.10, 1.46)$, for the cases $L = 0.5$ (a) and $L = 4$ (b).

3.4.1.3 Point P_3, $(\mathcal{A}_0, \mathcal{A}_1, \alpha_0^{(0)}) = (4.85, 2.10, 1.46)$.

Figure 3.9 shows results when the 1D case represented by point P_3 in $(\mathcal{A}_0, \mathcal{A}_1, \alpha^{(0)})$-space is perturbed at both boundaries, with no phase difference, as in (3.16). This case differs from the previous two: the region of two-way switching has shrunk considerably, to some small neighborhood of the point $(L, \delta) = (1, 0.5)$. As with the two other points though, the solution space complexity increases markedly as L increases: for $L \geq 1$, we find three solutions can coexist ($\boldsymbol{n}_1$, $\boldsymbol{n}_2$ and $\boldsymbol{n}_3$), while for $L \geq 4$, we again find four solutions that can coexist for a wide range of δ-values. This increase in solution complexity may again be illustrated by bifurcation diagrams as the bifurcation parameter δ is increased: Figure 3.10 shows the bifurcation diagrams for $L = 0.5$ and $L = 4$. As usual, the shorter domain length leads to a simple pitchfork bifurcation.

3.4.1.4 Point P_4, $(\mathcal{A}_0, \mathcal{A}_1, \alpha_0^{(0)}) = (2.20, 2.05, 1.18)$.

We are also curious about the system behavior when the point about which we perturb is located inside, on the lower side of the "switch region" (see Figure 3.1). Figure 3.11 shows results when the 1D case represented by point P_4 in $(\mathcal{A}_0, \mathcal{A}_1, \alpha^{(0)})$-space is perturbed at both boundaries, with no phase difference, as in (3.16). This case differs from the previous three: no two-way switching is achieved with our chosen switching protocol. As with the other three points though, the solution space complexity increases markedly as L increases: for $L \geq 3$, we again find four solutions that can coexist (but only for $\delta \geq 0.5$). This increase in solution complexity may again be illustrated by bifurcation diagrams as the bifurcation parameter δ is increased; however, we do not show these bifurcation diagrams here.

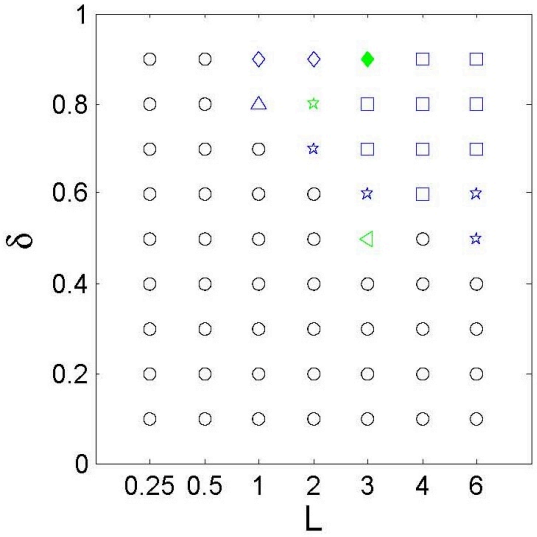

Figure 3.11 Switching results when perturbing the 1D case represented by point P_4, $(\mathcal{A}_0, \mathcal{A}_1, \alpha_0^{(0)}) = (2.20, 2.05, 1.18)$, according to (3.16).

3.4.2 Equal-amplitude Perturbations with Phase Difference

In this section, we consider the case with anchoring angles α_0, α_1 at lower and upper boundaries given by

$$\begin{aligned} \alpha_0 &= \alpha_0^{(0)} + \delta\cos(2\pi x/L + \phi), \\ \alpha_1 &= \alpha_0^{(0)} - \pi/2 + \delta\cos(2\pi x/L), \end{aligned} \tag{3.17}$$

as the perturbation amplitude δ and phase-shift ϕ vary. For each point in parameter space considered, motivated by the underlying application (which requires two-way switching for utility) we fix the domain length L at the "most promising" value indicated by the results of §3.4.1.

3.4.2.1 Point P_1, $(\mathcal{A}_0, \mathcal{A}_1, \alpha_0^{(0)}) = (5.41, 2.45, 1.40)$.

For this point, the (equal) best domain length in terms of achieving the largest window of two-way switching, as indicated by the results of §3.4.1, Figure 3.4, is $L = 0.5$. We therefore consider the influence of introducing a phase difference, ϕ, into the

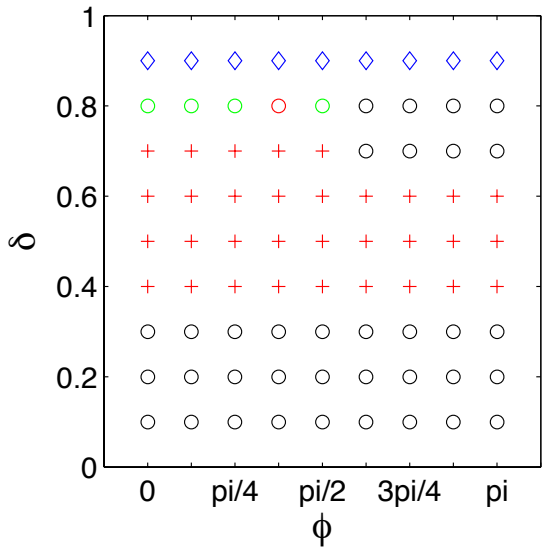

Figure 3.12 Switching results when perturbing the 1D case represented by point P_1, $(\mathcal{A}_0, \mathcal{A}_1, \alpha_0^{(0)}) = (5.41, 2.45, 1.40)$, according to (3.17). The domain length is fixed at $L = 0.5$.

anchoring variations on both boundaries, as indicated in (3.17) above, with L fixed at this value.

Figure 3.12 shows the results as the phase difference in boundary conditions (3.17), is increased from $\phi = 0$ to $\phi = \pi$. Note that for this and the subsequent points considered, the results for $\pi \leq \phi \leq 2\pi$ may be obtained by reflecting Figure 3.4 about $\phi = \pi$. Curiously, the results are almost independent of the phase difference, a sizeable window of two-way switching persisting for all values of ϕ tested. No pattern of increasing solution complexity emerges here: the third steady state $\boldsymbol{n}_3$ is always observed only for large δ, and no fourth steady state is found.

3.4.2.2 Point P_2, $(\mathcal{A}_0, \mathcal{A}_1, \alpha_0^{(0)}) = (5.50, 2.30, 1.46)$.

For this point, the best domain length in terms of achieving the largest window of two-way switching, as indicated by the results of §3.4.1, Figure 3.6, is again $L = 0.5$. Figure 3.13 shows the results as the phase difference in (3.17) is increased from $\phi = 0$ to $\phi = \pi$. In this case the window of two-way switching shrinks as ϕ is increased, and

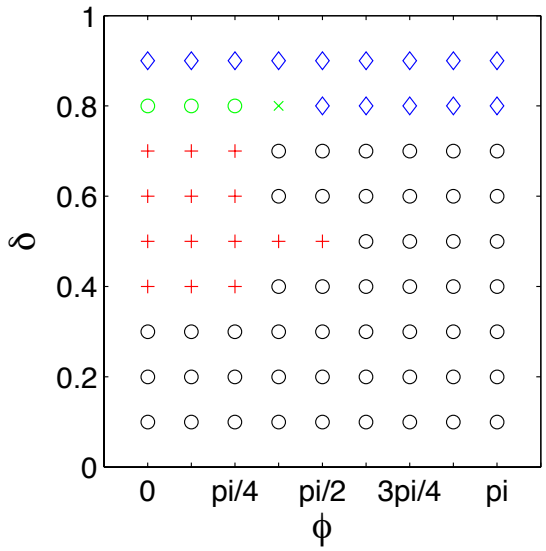

Figure 3.13 Switching results when perturbing the 1D case represented by point P_2, $(\mathcal{A}_0, \mathcal{A}_1, \alpha_0^{(0)}) = (5.50, 2.30, 1.46)$, according to (3.17). The domain length is fixed at $L = 0.5$.

disappears. Otherwise, the behavior is similar to that observed for point P_1 above: there is no evidence of increasing solution complexity as ϕ is varied; $\boldsymbol{n}_3$ is found only at large δ; and no fourth steady state is ever found.

3.4.2.3 Point P_3, $(\mathcal{A}_0, \mathcal{A}_1, \alpha_0^{(0)}) = (4.85, 2.10, 1.46)$.

For this point, two-way switching was observed in the results of §3.4.1 only for the domain length $L = 1$ (see Figure 3.9), hence we fix $L = 1$ here.

Figure 3.14 shows the results as the phase difference in (3.17) is increased from $\phi = 0$ to $\phi = \pi$. As with point P_1, little variation with ϕ is observed. The small window of two-way switching persists until $\phi = \pi/2$, after which it vanishes. The steady state $\boldsymbol{n}_3$ appears at the same δ value for all phase shifts ϕ ($\delta = 0.7$), in coexistence with $\boldsymbol{n}_1$ and $\boldsymbol{n}_2$ for $0 \leq \phi \leq \pi/2$, and in coexistence with $\boldsymbol{n}_2$ only for $\phi > \pi/2$ (so the bifurcation structure changes slightly as ϕ is increased).

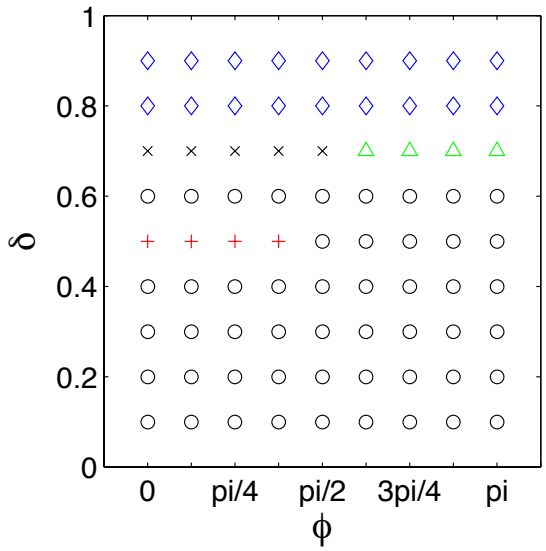

Figure 3.14 Switching results when perturbing the 1D case represented by point P_3, $(\mathcal{A}_0, \mathcal{A}_1, \alpha_0^{(0)}) = (4.85, 2.10, 1.46)$, according to (3.17). The domain length is fixed at $L = 1$.

3.4.2.4 Point P_4, $(\mathcal{A}_0, \mathcal{A}_1, \alpha_0^{(0)}) = (2.20, 2.05, 1.18)$.

For this point, no two-way switching was observed in the results of §3.4.1 (see Figure 3.11) and we just fix $L = 1$ here.

Figure 3.15 shows the results as the phase difference in (3.17) is increased from $\phi = 0$ to $\phi = \pi$. As with point P_1, little variation with ϕ is observed. The steady state $\boldsymbol{n}_3$ appears at the same δ value for all phase shifts ϕ ($\delta = 0.8$), in coexistence with $\boldsymbol{n}_1$ and $\boldsymbol{n}_2$ for $0 \leq \phi \leq \pi/2$.

To conclude, though we carried out only limited tests, it does not appear that introducing phase difference into the boundary conditions leads to increased two-way switching.

3.4.3 Perturbation at One Boundary Only

In this section, we investigate the effects of anchoring variations at one bounding surface only (we choose the lower surface). The anchoring angles imposed when

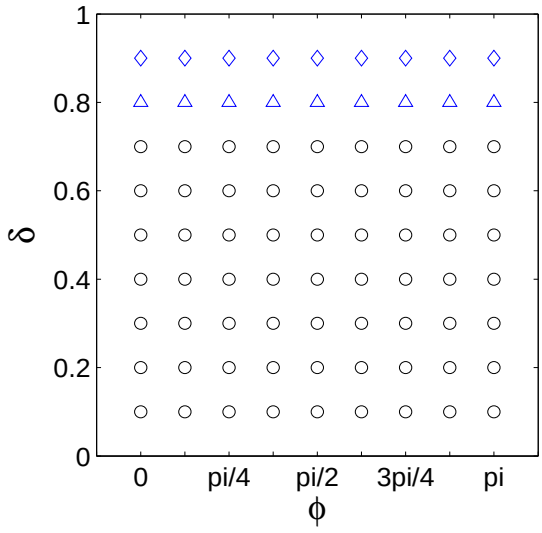

Figure 3.15 Switching results when perturbing the 1D device represented by point P_4, $(A_0, A_1, \alpha_0^{(0)}) = (2.20, 2.05, 1.18)$. The device length is fixed at $L = 1$, while δ and ϕ are allowed to vary.

solving (3.11)–(3.13) are

$$\alpha_0 = \alpha_0^{(0)} + \delta\cos(2\pi x/L), \quad \alpha_1 = \alpha_0^{(0)} - \pi/2. \tag{3.18}$$

3.4.3.1 Point P_1, $(\mathcal{A}_0, \mathcal{A}_1, \alpha_0^{(0)}) = (5.41, 2.45, 1.40)$.

Figure 3.16 shows that, in line with our earlier results, increasing the domain length, L, is associated with increasing solution complexity; though the switching obtained is less complex than in §3.4.1 where both boundaries are perturbed. No two-way switching is ever found, nor any switching cycles, therefore, in this instance at least, perturbing just the one boundary does not appear to be advantageous.

3.4.3.2 Point P_2, $(\mathcal{A}_0, \mathcal{A}_1, \alpha_0^{(0)}) = (5.50, 2.30, 1.46)$.

Figure 3.17 shows the results of a perturbation represented by (3.18) to the anchoring conditions on the lower boundary only, the unperturbed case being represented by point P_2 in the 1D problem. The same general observations as for point P_1 above hold: again, increasing the domain length, L, is clearly associated with increasing

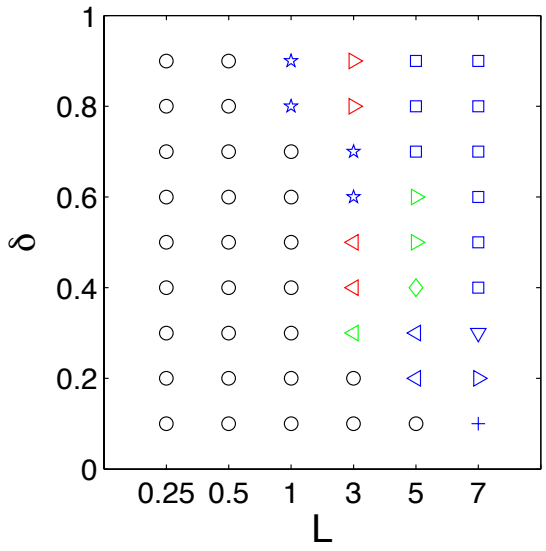

Figure 3.16 Switching results when perturbing the 1D case represented by point P_1, $(\mathcal{A}_0, \mathcal{A}_1, \alpha_0^{(0)}) = (5.41, 2.45, 1.40)$, according to (3.18). The lower boundary only is perturbed, and δ and L vary.

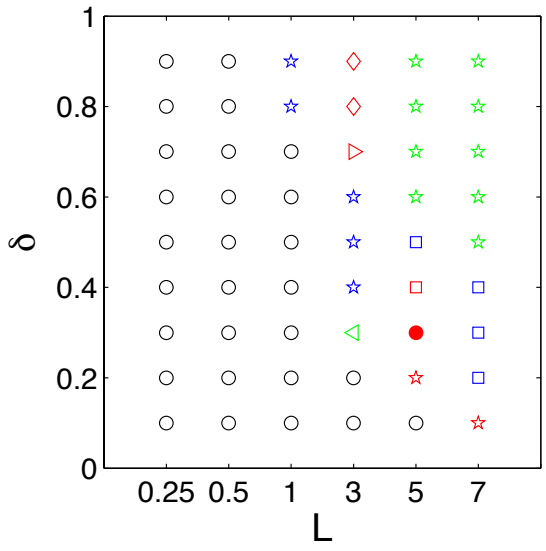

Figure 3.17 Switching results when perturbing the 1D case represented by point P_2, $(\mathcal{A}_0, \mathcal{A}_1, \alpha_0^{(0)}) = (5.50, 2.30, 1.46)$, according to (3.18). The lower boundary only is perturbed, and δ and L vary.

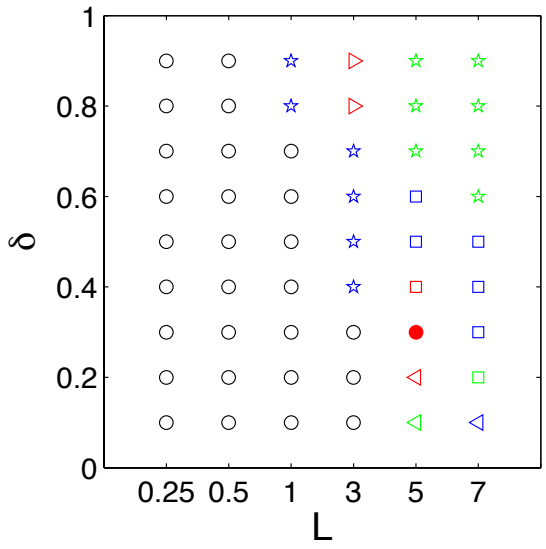

Figure 3.18 Switching results when perturbing the 1D case represented by point P_3, $(\mathcal{A}_0, \mathcal{A}_1, \alpha_0^{(0)}) = (4.85, 2.10, 1.46)$, according to (3.18). The lower boundary only is perturbed, and δ and L vary.

solution complexity, but behavior is overall less complex than in §3.4.1 where both boundaries are perturbed. No two-way switching or switching cycles are found for any (L, δ)-values tested, therefore for P_2 this type of boundary perturbation also does not lead to desired two-way switching.

3.4.3.3 Point P_3, $(\mathcal{A}_0, \mathcal{A}_1, \alpha_0^{(0)}) = (4.85, 2.10, 1.46)$.

Figure 3.18 shows the results for point P_3 in the 1D problem. This case behaves similarly to points P_1 and P_2 above, with increasing L leading to increased complexity, but with no useful two-way or cyclic switching found.

3.5 Discussion and Conclusions

We have taken a basic but promising 1D model for a bistable LCD device [9], and investigated how it behaves under perturbations to the anchoring boundary conditions (specifically, periodic perturbations to the anchoring angles at the flat bounding surfaces). Such perturbations to the anchoring angles could be due to

periodic chemical gradients imposed at the surfaces, or may also be thought of as approximating a device with periodic topographical variations. The study of such variations is important for two reasons: firstly, it may provide useful indications of how to tune boundaries to create a workable bistable device of this kind, which improves on the simpler 1D model proposed in Chapter 2; and secondly, it will provide insight into the robustness of the underlying 1D device to engineering imperfections.

Our results are presented for a few chosen sample points in the space of surface energies $\mathcal{A}_0$, $\mathcal{A}_1$, at the upper and lower bounding surfaces respectively, and unperturbed anchoring angle $\alpha_0^{(0)}$ at the lower bounding surface, as outlined in §3.2.3 and §3.3. The motivation for choosing these test points was that they lie nearby the most promising region of parameter space for the 1D model, but when unperturbed, do not permit two-way switching (Chapter 2). Perturbing a 1D device based on these points therefore gives some insight into whether 2D effects can lead to improvements over the 1D results. The unperturbed anchoring angle at the upper bounding surface, $\alpha_1^{(0)}$, is fixed by (3.14). Both anchoring angles are systematically perturbed according to three different protocols, described in §3.4.1 (in-phase, variable-amplitude, variable wavelength perturbations to both angles), §3.4.2 (variable phase, variable amplitude, fixed wavelength perturbations to both angles) and §3.4.3 (variable amplitude, variable wavelength perturbations to one angle only). Where both boundaries are perturbed, the perturbation amplitude, δ, is the same at each boundary; where only the lower boundary is perturbed, the phase difference, ϕ, is zero by default. Since only two of the three variables δ, L (domain length) and ϕ are perturbed in any set of experiments, our results on the steady states found and switching between them can be easily represented graphically by 2D parametric plots.

For all cases studied, we find that the perturbations lead to surprisingly rich behavior when compared with the 1D case. As we would expect, for sufficiently small δ, the results are close to those found in 1D: only two stable steady states,

with no two-way switching. However, for a given L we find a threshold value δ^* at which a bifurcation occurs and new steady states are found. This threshold value δ^* decreases as L increases. Depending on the value of L, the new steady state(s) may either replace the continuations of the original steady states $\boldsymbol{n}_1$ and $\boldsymbol{n}_2$ (a simple pitchfork bifurcation; Figures 3.5(a), 3.7(a), 3.10(a)), or else coexist with them (a saddle-node bifurcation; Figures 3.5(b), 3.7(b), 3.10(b)). Though a full bifurcation study was not performed, our results indicate that short domains (small L) lead to a pitchfork bifurcation in which bistability yields to monostability, while long domains give a more complex bifurcation structure with folds, in which multiple distinct steady states can coexist (in the cases we considered, up to four states were found simultaneously). The bifurcation to tri- and tetrastability can occur at very small δ^* for the largest L's considered. Somewhat surprisingly, introducing a phase difference between perturbations at the two boundaries does not have a significant effect on the results obtained, at least for the domains considered.

On the one hand, our results indicate that long-wavelength perturbations of even very small amplitude may introduce significant complexity, in particular multiple stable steady states, but with a lack of switching between them. While interesting from a scientific point of view, this finding also has a practical consequence, since it suggests that such perturbations are not useful if a reliable bistable device with two-way switching is desired. This finding also suggests that an unperturbed device, of the kind discussed in Chapter 2, may be unstable if the domain length is large; in large domains, multistability and undesired complexity may be a possibility.

On the other hand, we do find a sizeable set of boundary perturbations for which two-way switching is found between states $\boldsymbol{n}_1$ and $\boldsymbol{n}_2$, for parameters for which two-way switching is not possible in the unperturbed case. Even more interestingly, we find that two-way switching between the newly-found $\boldsymbol{n}_3$ state and the $\boldsymbol{n}_2$ state, as well as cyclic switching $\boldsymbol{n}_1 \to \boldsymbol{n}_3 \to \boldsymbol{n}_2 \to \boldsymbol{n}_1$, may occur. Therefore, we find

significant potential utility of the boundary perturbations, particularly of shorter wavelengths, provided one can make boundary modifications of wavelength comparable to or smaller than the device thickness, and of reasonable amplitude. Presumably the finite-sized amplitude of such perturbations would be sufficient to destroy the undesired sensitivity to long-wavelength, small amplitude perturbations noted above.

In this work, we have considered a three dimensional parameter space defined by ($\mathcal{A}_0$, $\mathcal{A}_1$, $\alpha_0^{(0)}$). It is clearly difficult to analyze this large space in detail by the present methods, and we cannot claim that the results found at the considered isolated points cover the whole range of possible solutions. For example, we found that up to four steady states can co-exist in some cases; however even more complex scenarios with a larger number of stable solutions are possible. Despite the limitations of the presented analysis, our results do suggest that improvements from the unperturbed 1D configurations are possible; however, the extent of these improvements may depend on the choice of physical parameters (anchoring strengths and angles). In addition, our results strongly suggest that short wavelength perturbations are more promising if formulation of a bistable switchable device is desired.

Our results are also interesting when compared to theoretical simulations of the so-called ZBD (Zenithal Bistable Device) [3]. In that device, a 2D model is found to permit bistability and two-way switching via boundary perturbations (geometric, for the ZBD); but one of the two steady states has a disclination. Our model suggests that a truly 2D bistable switchable device may in fact be possible without any disclinations.

CHAPTER 4

1D MODEL WITH NON-UNIFORM FIELD

In the models studied so far in this dissertation, several simplifying assumptions were made to obtain a more tractable model, one of which is the assumption that the electric field is uniform throughout the device. In this chapter, we formulate and investigate a model that accounts for the interaction between the field and the device. We restrict attention here to a simple 1D model, where the electric field varies only in the direction parallel to the bounding plates, addressing in particular the question of how large the deviation from uniformity may be.

In this chapter, only the steady model is derived and studied. Consideration of time-dependent effects in this coupled problem is beyond the scope of the present work.

4.1 Modeling and Parameters

As stated above, we consider a simple 1D variable-field model, in which the director field $\boldsymbol{n}$ is given by

$$\boldsymbol{n} = (\sin\theta, 0, \cos\theta), \tag{4.1}$$

where $\theta(z^*)$ is the angle made by the director with the z-axis. We consider a device consisting of a thin film of NLC which is sandwiched between the bounding surfaces $z^* = 0$ and $z^* = h^*$. The electric field is no longer assumed uniform, but is given by the gradient of a potential function $\phi^*(z^*)$:

$$\boldsymbol{E}^* = (0, 0, \phi^*_{z^*}).$$

We assume that the two bounding surfaces are each at uniform potential:

$$\phi^*(0) = 0, \quad \phi^*(h^*) = P^*.$$

The free energy of the liquid crystal layer, in the presence of an applied electric field and with specified anchoring conditions at each bounding surface, has several contributions. The bulk free energy density consists of elastic, dielectric and flexoelectric contributions W_e^*, W_d^*, W_f^*, and in our 1D model with the nonuniform field assumption these are given by

$$2W_e^* = K_1^*(\nabla^* \cdot \boldsymbol{n})^2 + K_3^*((\nabla^* \times \boldsymbol{n}) \times \boldsymbol{n})^2, \tag{4.2}$$

$$2W_d^* = -\varepsilon_0^*\varepsilon_\perp(\boldsymbol{E}^*)^2 - \varepsilon_0^*(\varepsilon_\parallel - \varepsilon_\perp)(\boldsymbol{n} \cdot \boldsymbol{E}^*)^2, \tag{4.3}$$

$$W_f^* = -\boldsymbol{E}^* \cdot (e_1^*(\nabla^* \cdot \boldsymbol{n})\boldsymbol{n} + e_3^*(\nabla^* \times \boldsymbol{n}) \times \boldsymbol{n}), \tag{4.4}$$

where K_1^* and K_3^* are elastic constants, ε_0^* is the permittivity of free space, $\varepsilon_\parallel$ and $\varepsilon_\perp$ are the relative dielectric permittivities parallel and perpendicular to the long axis of the nematic molecules, and e_1^* and e_3^* are flexoelectric constants. Note that the first term appearing in the dielectric energy density (on the right-hand side of (4.3)) played no role in the preceding uniform field analysis. With the director field $\boldsymbol{n}$ as given by (4.1), with $\theta = \theta(z^*)$, and the common simplifying assumption $K_1^* = K_3^* = K^*$, the total bulk free energy density $W^* = W_e^* + W_d^* + W_f^*$ simplifies. Introducing the nondimensional forms $W = K^*W^*/h^{*2}$ and $z = z^*/h^*$,

$$W = \frac{\theta_z^2}{2} - \mathcal{D}\phi_z^2(\omega + \cos^2\theta) + \frac{\mathcal{F}\theta_z\phi_z}{2}\sin 2\theta, \tag{4.5}$$

where

$$\mathcal{D} = \frac{h^{*2}E^{*2}\varepsilon_0^*(\varepsilon_\parallel - \varepsilon_\perp)}{2K^*}, \quad \mathcal{F} = \frac{h^*E^*(e_1^* + e_3^*)}{K^*}, \tag{4.6}$$

$$\omega = \frac{\varepsilon_\perp}{\varepsilon_\parallel - \varepsilon_\perp}, \quad \varepsilon_\parallel \sim 9, \quad \varepsilon_\perp \sim 3 \tag{4.7}$$

are dimensionless constants. Though the definitions of $\mathcal{D}$ and $\mathcal{F}$ in (4.6) are as usual, the factor E^* appearing in them should here be understood as

$$E^* = P^*/h^*. \tag{4.8}$$

Both $\mathcal{D}$ and $\mathcal{F}$ are $O(1)$. $\mathcal{D}$ is a dielectric coefficient and $\mathcal{F}$ measures the strength of the flexoelectric effect relative to elasticity.

The surface energy remains the same as defined by Rapini & Papoular; if $g^*_{\{0,h^*\}} = (K^*/h^*)g_{\{0,1\}}$ are the surface energies per unit length at the boundaries $z^* = 0,\ h^*$, then

$$g_{0,1} = \frac{\mathcal{A}_{\{0,1\}}}{2}\sin^2(\theta - \alpha_{\{0,1\}}), \quad \text{where} \quad \mathcal{A}_{\{0,1\}} = \frac{h^* A^*_{\{0,h^*\}}}{K^*}. \tag{4.9}$$

As usual, $A^*_{\{0,h^*\}}$ are the anchoring strengths at $z^* = 0,\ h^*$ and $\alpha_{\{0,1\}}$ are the preferred angles.

The total (dimensionless) free energy for the system is given by

$$J = \int_0^1 W(\theta, \theta_z, \phi, \phi_z)\, dz + g_0(\theta)|_{z=0} + g_1(\theta)|_{z=1}\,.$$

The standard Euler-Lagrange variational calculus approach is introduced to consider the variation induced in J by small variations in θ and ϕ:

$$\theta(z) \to \theta(z) + \epsilon\eta(z) \quad \text{and} \quad \phi(z) \to \phi(z) + \lambda\mu(z),$$

where $0 < \epsilon, \lambda \ll 1$.

Considering J as a function of θ, θ_z, ϕ and ϕ_z, we compute the first variation in J, assuming the Dirichlet conditions $\phi(0) = 0$, $\phi(1) = 1$,

$$J_1 = \epsilon\int_0^1 \eta[W_\theta - (W_{\theta_z})_z]dz + \lambda\int_0^1 \mu[W_\phi - (W_{\phi_z})_z]dz$$

$$+ \epsilon\eta(g_{1\theta} + W_{\theta_z})_{z=1} + \epsilon\eta(g_{0\theta} - W_{\theta_z})_{z=0}.$$

At equilibrium, $O(\epsilon)$ and $O(\lambda)$ must vanish independently for all sufficiently smooth variations $\eta(z)$ and $\mu(z)$. This condition gives rise to the following governing equations:

$$\theta_{zz} - \mathcal{D}\phi_z^2 \sin 2\theta + \frac{\mathcal{F}}{2}\phi_{zz} \sin 2\theta = 0, \tag{4.10}$$

$$\frac{\mathcal{F}}{2}\theta_{zz} \sin 2\theta + \mathcal{F}\theta_z^2 \cos 2\theta - 2\mathcal{D}\phi_{zz}(\cos^2\theta + \omega) + 2\mathcal{D}\phi_z\theta_z \sin 2\theta = 0, \tag{4.11}$$

and boundary conditions:

$$\frac{\mathcal{A}_0}{2} \sin(2(\theta - \alpha_0)) - \theta_z - \frac{\mathcal{F}}{2}\phi_z \sin(2\theta) = 0, \qquad z = 0 \tag{4.12}$$

$$\frac{\mathcal{A}_1}{2} \sin(2(\theta - \alpha_1)) + \theta_z + \frac{\mathcal{F}}{2}\phi_z \sin(2\theta) = 0, \qquad z = 1 \tag{4.13}$$

for θ; and conditions

$$\phi = 0 \quad \text{on} \quad z = 0, \qquad \text{and} \qquad \phi = 1 \quad \text{on} \quad z = 1, \tag{4.14}$$

for ϕ.

This coupled system of two second order differential equations for $\theta(z)$ and $\phi(z)$ replaces (2.15) for the 1D problem with uniform field. We solve it numerically to investigate the importance of nonuniformities in the electric field.

4.2 Numerical Method

As derived above (4.10)-(4.14), the nonlinear boundary value problem with two variables (θ, ϕ) can be solved numerically with built-in solvers by MATLAB.

We first rewrite (4.10)-(4.14) as a vector system of four first order ODEs for $\theta, \theta_z, \phi, \phi_z$, then apply the built-in routine "bvp4c" provided by MATLAB,

sol = bvp4c (odefun, bcfun, solinit).

"bvp4c" has only three arguments: a function "odefun" for evaluating the ODEs, a function "bcfun" for evaluating the residual in the boundary conditions, and a structure "solinit" that provides a guess for a mesh and initial solutions on this mesh. The ODEs are handled exactly as in the MATLAB IVP solvers. The initial guess solution "solinit" in terms of (θ_0, ϕ_0) is constructed by assuming a linear approximation for both θ and ϕ consistent with the boundary conditions. Hence, we assume $\phi_0 = z$ for all cases; for θ_0, if surface anchoring is fairly strong, we take $\theta_0 = \alpha_0 + (\alpha_1 - \alpha_0)z$, but if anchoring is weak, we base our initial guess on the steady-state uniform-field numerical solutions.

We first consider how the uniform field approximation compares with this new variable-field model in the cases of likely relevance (within, or close to, the "switching region" constructed for the 1D problem, as shown in Figure 3.1). Thus, we first compare the model solutions for the points, P_1-P_4, introduced in Chapter 3, under the usual conditions $\mathcal{D} = 2.5$, $\mathcal{F} = -5.0$ (these values again give $\Upsilon = 10$ in (2.7)). Finding fairly good agreement between uniform and nonuniform cases for all four points under these conditions, we then proceed to investigate more extreme cases, in order to determine when the uniform field approximation is no longer acceptable.

4.3 Results

Since our parameter space is too large (even for the 1D problem considered here) to carry out an exhaustive numerical investigation, we carry out a limited but systematic comparison of the uniform field problem (4.10)-(4.14) and the nonuniform field problem (2.15) to see when and by how much the results differ. Throughout this investigation, we consider only the steady problem, as explained in §4.1, thus we address the question of by how much the results differ under a steady applied field with given values of $\mathcal{F}$ and $\mathcal{D}$.

We first focus attention on the four points P_1-P_4 in $(\mathcal{A}_0, \mathcal{A}_1, \alpha)$-parameter space studied in the previous chapter, under the standard "switching conditions" ($\mathcal{F} = -5.0, \mathcal{D} = 2.5$, so that the material parameter $\Upsilon = \mathcal{F}^2/\mathcal{D} = 10$; see (2.7)), but now for a steady rather than transient applied field.

For the point P_1, we then compare model solutions under a wider range of conditions, corresponding to different values of Υ (materials respond differently to the applied field).

Finally, we also consider how the variation of anchoring boundary conditions (weak versus strong anchoring at one or both bounding surfaces) may affect the model results.

4.3.1 Standard Switching Conditions and Material Properties

We first present the results for cases of likely industrial relevance. We consider the devices represented by points P_1-P_4 in $(\mathcal{A}_0, \mathcal{A}_1, \alpha)$-space (see Chapter 3, Figure 3.1) and compare the results of the system (4.10)-(4.14) to those of (2.15). Figures 4.1-4.4 show the comparison of the models for these examples. In all cases, the steady states θ_1, θ_2 for the uniform field model are represented by dash-dot curves (blue and green, respectively), while the director angle solutions for the non-uniform field model are represented by solid red curves. The electric potential ϕ for the non-uniform field case is represented by a dash blue curve, while the dotted dark line of unit gradient represents the electric potential $\phi = z$ for the uniform field.

For points P_1-P_3, bistable states (θ_1, θ_2) exist for uniform field problem. Each of Figures 4.1-4.3 contains two subfigures: In the left-hand subfigure, the steady state θ_1 was taken as the initial guess for the non-uniform field solution θ; while in the right-hand subfigure, θ_2 was taken as the initial guess. As anticipated, we find that the solution of (4.10)-(4.14) for θ converges to different states for these different initial guesses. The deviations of the non-uniform field solutions for θ from

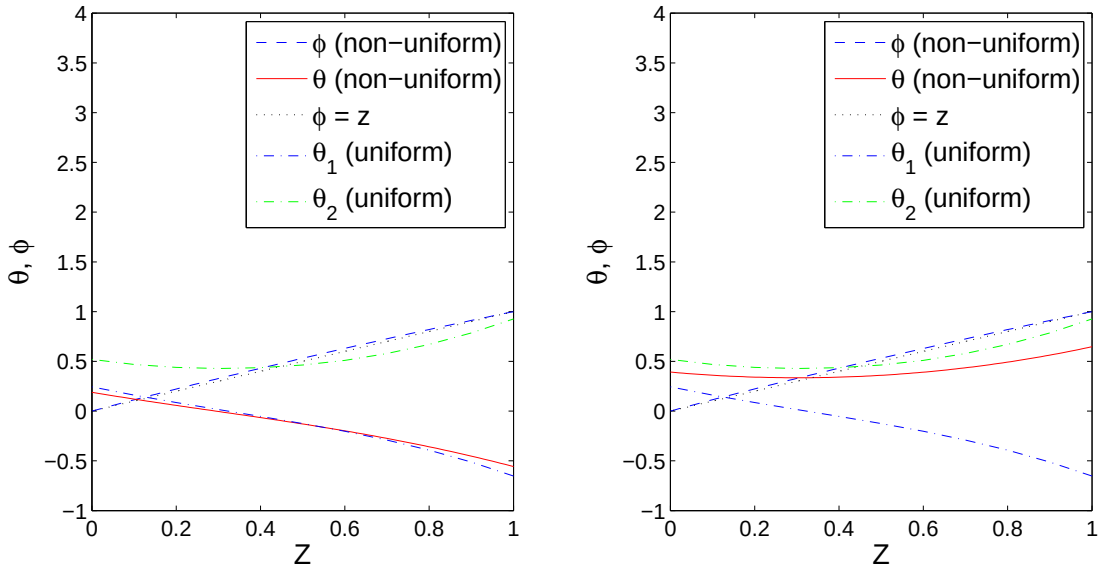

Figure 4.1 Solutions of non-uniform field system (4.10)-(4.14) for point P_1, $(\mathcal{A}_0, \mathcal{A}_1, \alpha_0^{(0)}) = (5.41, 2.45, 1.40)$, compared with uniform field system (2.15), where $\mathcal{F} = -5.0$ and $\mathcal{D} = 2.5$.

the uniform field solutions θ_1 and θ_2 are always acceptably small, however; and in all cases, the non-uniform field solution for ϕ is very close to linear. For the point P_4 however (Figure 4.4), the bistability is destroyed even in the uniform field problem. Only one steady state exists for both uniform and non-uniform field problems. The deviation of the non-uniform field problem from the uniform field approximation is tiny.

4.3.2 Effect of Changing the Parameter $\mathcal{F}$

In this subsection, we carry out a more general investigation to determine the effect of varying the parameter $\mathcal{F}$ (defined in (4.6)) on the field nonuniformities. For a given device, this may be thought of as increasing the applied potential drop across the bounding surfaces. To keep the investigation manageable, we consider only the device represented by the point P_1, and we keep the material parameter $\Upsilon = \mathcal{F}^2/\mathcal{D}$ fixed at the usual value 10. Figure 4.5 summarizes the results in a simple graph,

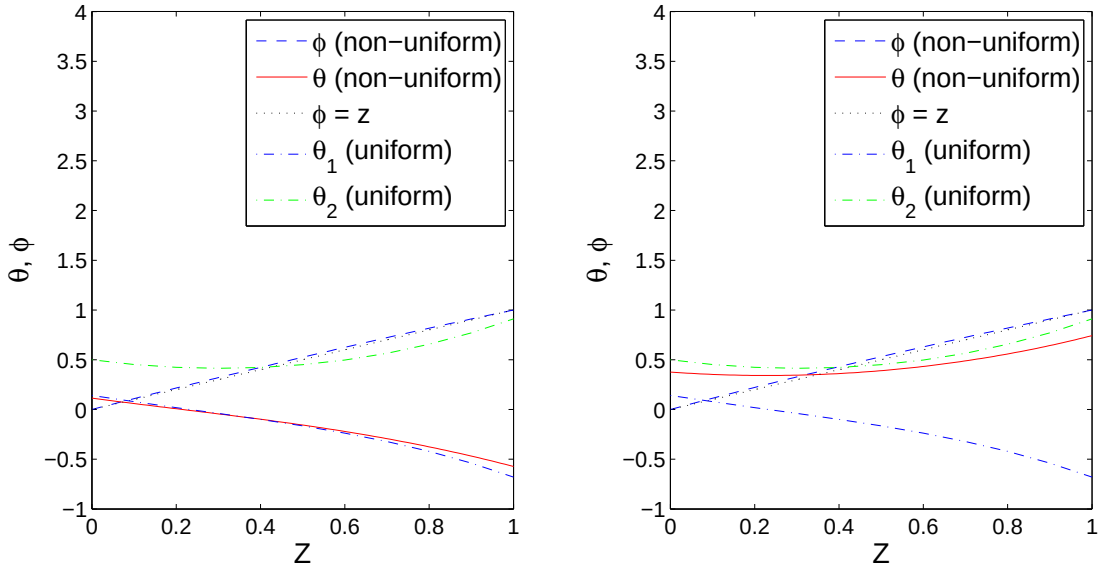

Figure 4.2 Solutions of non-uniform field system (4.10)-(4.14) for point P_2, $(\mathcal{A}_0, \mathcal{A}_1, \alpha_0^{(0)}) = (5.50, 2.30, 1.46)$, compared with uniform field system (2.15), where $\mathcal{F} = -5.0$ and $\mathcal{D} = 2.5$.

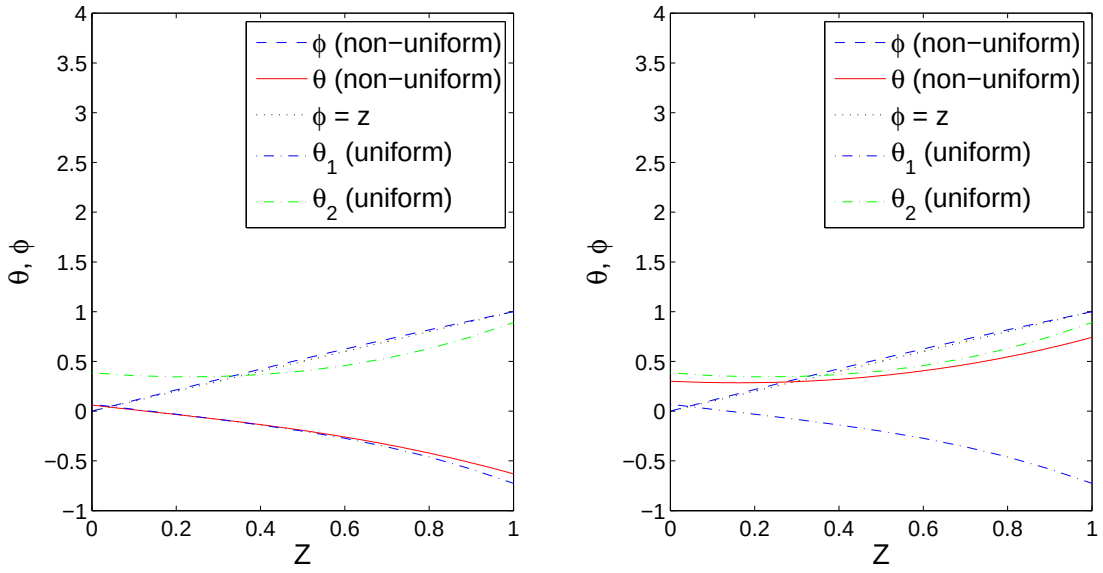

Figure 4.3 Solutions of non-uniform field system (4.10)-(4.14) for point P_3, $(\mathcal{A}_0, \mathcal{A}_1, \alpha_0^{(0)}) = (4.85, 2.20, 1.46)$, compared with uniform field system (2.15), where $\mathcal{F} = -5.0$ and $\mathcal{D} = 2.5$.

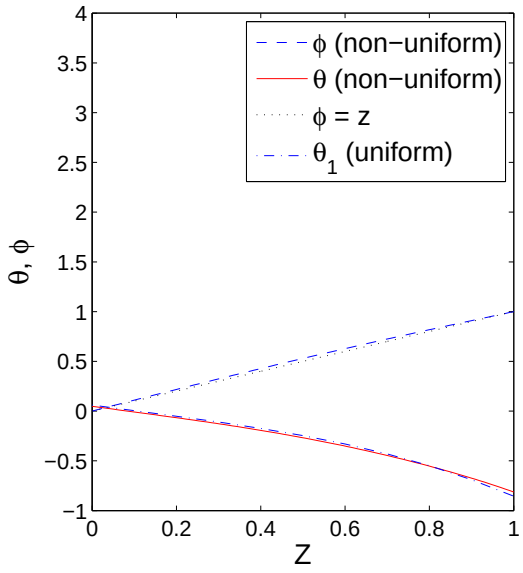

Figure 4.4 Solutions of non-uniform field system (4.10)-(4.14) for point P_4, $(\mathcal{A}_0, \mathcal{A}_1, \alpha_0^{(0)}) = (2.20, 2.05, 1.18)$, compared with uniform field system (2.15), where $\mathcal{F} = -5.0$ and $\mathcal{D} = 2.5$.

plotting the maximal deviation of the electric potential between the plates from the linear state as $\mathcal{F}$ increases:

$$Deviation := \sqrt{\sum_{i=1}^{N} \left(\frac{(\phi_i - z_i)^2)}{N} \right)}, \tag{4.15}$$

where ϕ_i is the discretization of the electric potential ϕ between the plates at the ith grid point; z_i is the discretization of the linear state $\phi = z$, and N is the total number of grid points. Interestingly, in this case the deviation is largest for small values of $\mathcal{F}$, decreasing and approaching a small constant value as $\mathcal{F}$ increases.

Figure 4.6 shows an example of a relatively large deviation of the electric potential ϕ from the uniform field case. For this figure, $\mathcal{F}$ was chosen to be -1.0, corresponding to the largest deviation we computed (though likely not the largest possible deviation). As usual, Υ was fixed at the value 10. We note that this value of $\mathcal{F}$ is, in general, too small to achieve the device switching, and that therefore this case is likely not industrially-relevant.

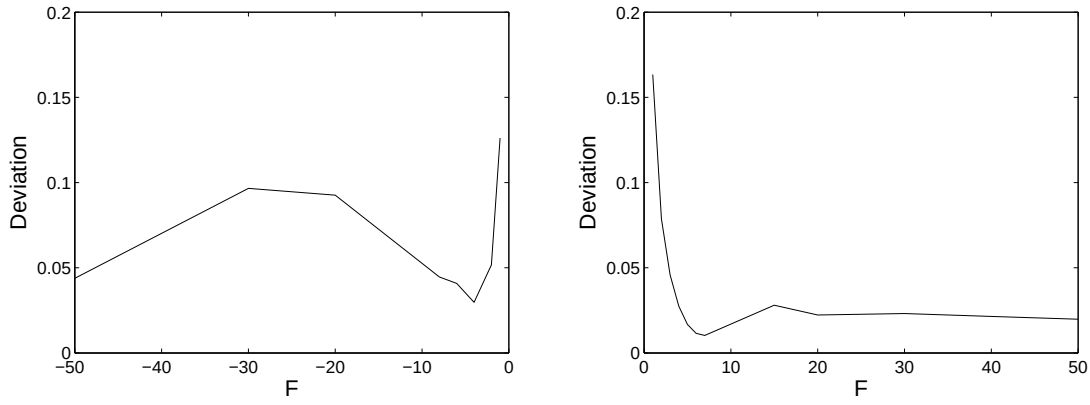

Figure 4.5 Deviation of the electric potential between the plates from the linear state for the device represented by point P_1, $(\mathcal{A}_0, \mathcal{A}_1, \alpha_0^{(0)}) = (5.41, 2.45, 1.40)$, where $\Upsilon = \mathcal{F}^2/\mathcal{D}$ is fixed at 10 and $\mathcal{F}$ varies.

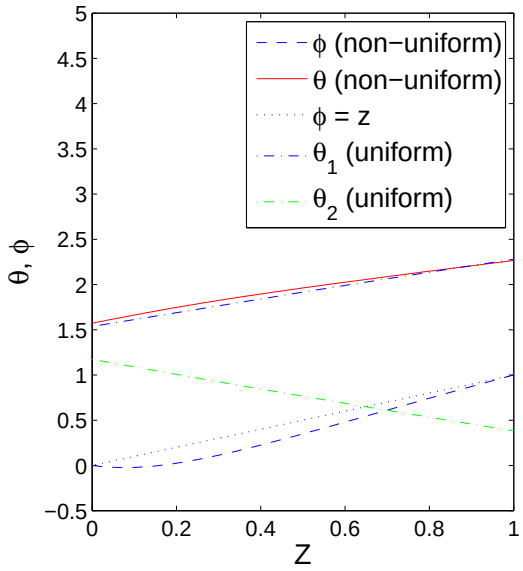

Figure 4.6 Solutions of non-uniform field system (4.10)-(4.14) for point P_1, $(\mathcal{A}_0, \mathcal{A}_1, \alpha_0^{(0)}) = (5.41, 2.45, 1.40)$, compared with uniform field system (2.15), where $\mathcal{F} = -1.0$ and $\mathcal{D} = 0.1$.

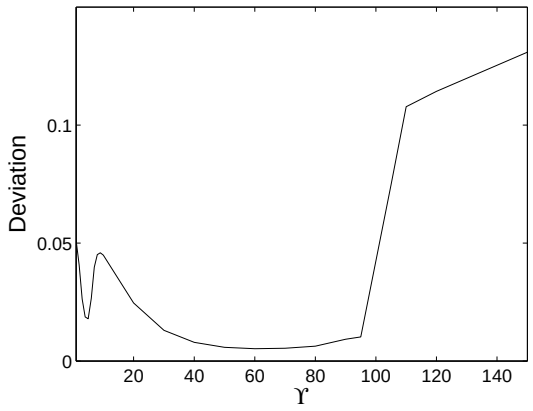

Figure 4.7 Deviation of the electric potential between the plates from the linear state for the device represented by point P_1, $(\mathcal{A}_0, \mathcal{A}_1, \alpha_0^{(0)}) = (5.41, 2.45, 1.40)$, where $\mathcal{F}$ is fixed at the value -5.0 and the material parameter $\Upsilon = \mathcal{F}^2/\mathcal{D}$ varies.

4.3.3 Effect of Changing Material Properties

In this subsection, we keep the applied field parameter $\mathcal{F}$ fixed at the value -5.0 and change the material parameter $\Upsilon = \mathcal{F}^2/\mathcal{D}$. Again, to keep the computations manageable we focus attention on the single point P_1 in our parameter space of anchoring conditions. The plot in Figure 4.7 summarizes the results in a simple graph. The deviations (defined in (4.15)) of the electric potential between the plates from the linear state are smallest for small values of Υ, and increase as Υ increases, until a local maximum deviation is reached, after which the deviation decreases again. The small deviation at small values of Υ could be understood in terms of a large (positive) dielectric anisotropy. NLC molecules respond very strongly to even a small applied field, aligning almost perfectly (unless surface anchoring is very strong, which it is not in these computations). Since the director field of the NLC is aligned very nearly perpendicular to the plates in both uniform and nonuniform field cases, one would expect little influence on the electric potential.

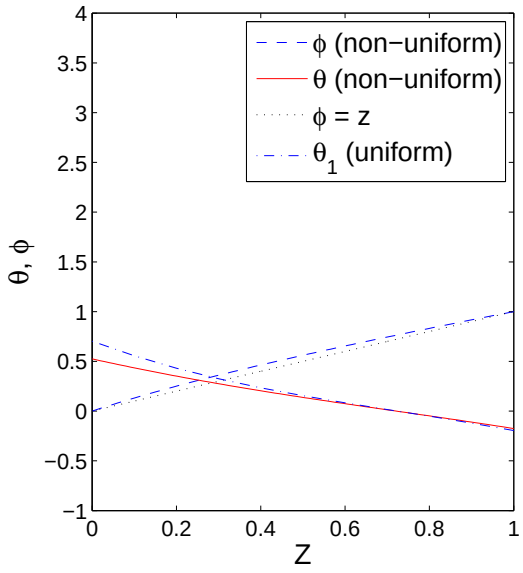

Figure 4.8 Solutions of non-uniform field system (4.10)-(4.14) for point P_5, $(\mathcal{A}_0, \mathcal{A}_1, \alpha_0^{(0)}) = (8.0, 8.0, 1.4)$, compared with uniform field system (2.15), where $\mathcal{F} = -5.0$ and $\mathcal{D} = 2.5$.

4.3.4 Variable Anchoring Conditions

Our studies so far have revealed a very strong dependence of results on the exact anchoring conditions assumed. Hence, we are motivated to explore more points in our parameter space of anchoring conditions than just the four points P_1-P_4 studied so far in this chapter.

Figure 4.8 shows the result of a new point P_5, $(\mathcal{A}_0, \mathcal{A}_1, \alpha_0^{(0)}) = (8.0, 8.0, 1.4)$, with relatively strong anchoring on both boundaries. Figure 4.9 shows the result of a new point P_6, $(\mathcal{A}_0, \mathcal{A}_1, \alpha_0^{(0)}) = (2.0, 8.0, 1.4)$, with weak anchoring on the bottom and strong anchoring on the top. Figure 4.10 shows the result of a new point P_7, $(\mathcal{A}_0, \mathcal{A}_1, \alpha_0^{(0)}) = (8.0, 2.0, 1.4)$, with strong anchoring on the bottom and weak on the top. In all these cases, bistability is destroyed even in the uniform field problem and the solutions of non-uniform and uniform field systems are close.

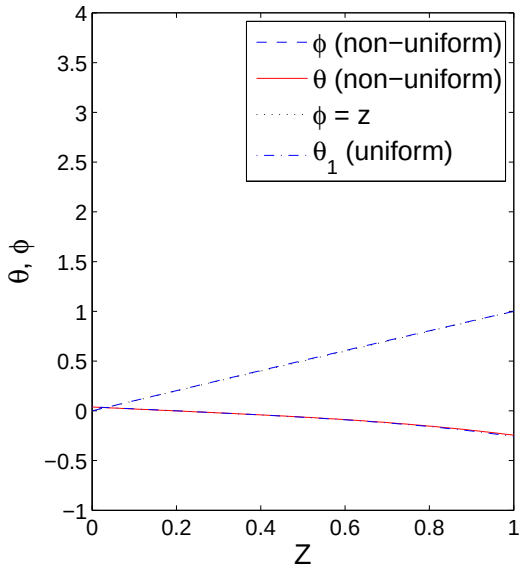

Figure 4.9 Solutions of non-uniform field system (4.10)-(4.14) for point P_6, $(\mathcal{A}_0, \mathcal{A}_1, \alpha_0^{(0)}) = (2.0, 8.0, 1.4)$, compared with uniform field system (2.15), where $\mathcal{F} = -5.0$ and $\mathcal{D} = 2.5$.

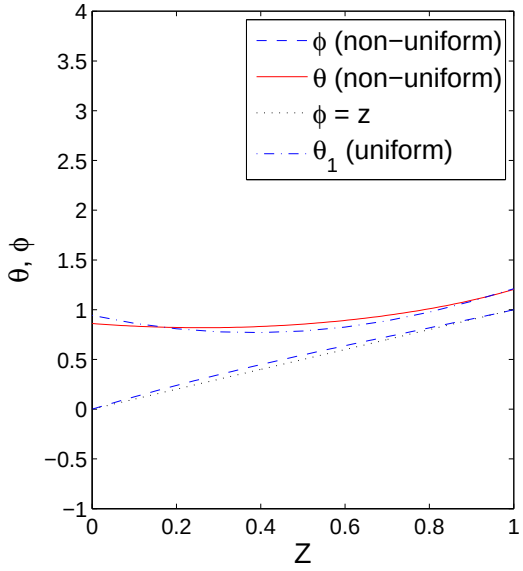

Figure 4.10 Solutions of non-uniform field system (4.10)-(4.14) for point P_7, $(\mathcal{A}_0, \mathcal{A}_1, \alpha_0^{(0)}) = (8.0, 2.0, 1.4)$, compared with uniform field system (2.15), where $\mathcal{F} = -5.0$ and $\mathcal{D} = 2.5$.

4.4 Discussion

In this chapter, we used our free energy minimization approach to derive the more general model governing the (steady state) director field configuration in the case where the NLC interacts with the applied field to make it non-uniform throughout the layer. The results of this chapter go some way towards justifying the use of our uniform field assumption made throughout most of the thesis. Though our investigations are admittedly limited, our results indicate that in the cases of likely industrial relevance, deviations of the electric field from the uniform case are small. Likewise, deviations between the director field solutions for the uniform and non-uniform field models are acceptably small in most cases. Sizeable deviations were noted only when the applied field was too small to effect switching (see Figure 4.5), or when the material parameter Υ was unphysically large (see Figure 4.7).

We note that the model and simulations presented in this chapter are limited to the steady-state case. Since transient effects will undoubtedly be important in the switching of any real bistable device, our conclusions here must be treated with caution as regards real appliations.

CHAPTER 5

FUTURE WORK

In this dissertation, we have considered a variety of mathematical models for a bistable Liquid Crystal Display (LCD) device, with different levels of complexity. We began in Chapter 2, by considering the simplest 1D model, with variation only in the direction perpendicular to the (parallel) bounding plates, and uniform applied field across these plates. This model was optimized for factors such as maximal robustness and visual contrast, minimal switching field and switching time, assuming perfect engineering control of surface anchoring properties.

In Chapter 3, we extended this model to two space dimensions, but in the simplest possible way: the geometry remained unchanged, with parallel bounding plates, but anchoring properties (in particular, the anchoring angles at upper and lower bounding plates) were allowed to vary along the plates. This model was investigated with regard to possible improvement in performance over the 1D model, and for bifurcations to other new steady states (which did not exist for the 1D model), which could warn of possible malfunction for a device based on the 1D model.

Finally, in Chapter 4, we questioned the assumption of uniform applied field, introducing a new (1D) model that allowed us to solve simultaneously for the electric potential within the NLC and the director orientation.

Much more could be done on this problem to study the viability of a bistable device based on these principles. We outline just a few possible directions here. Firstly, a more detailed investigation of the 2D problem formulated in Chapter 3 should be carried out. Due to the computational intensity of this problem (a very large possible parameter space), we were able to focus attention only on a very limited subset of parameter space, and we studied only a limited class of perturbations. In

particular, though our model is intended to give some sense of how topographical variations in the bounding surfaces might affect the 1D results, we have not studied true topographical variations. The perturbed anchoring angles in our model provide only a crude approximation to variable boundary topography. It should not be too challenging to formulate and solve a model that takes true account of arbitrary variable topography. Along the same lines, in addition to allowing the anchoring angles (or topography) to vary, it is also possible to create gradients in surface energies along the bounding surfaces. This would be another possible way of controlling the steady states and their switching properties, which it might prove profitable to study in future.

For the non-uniform field formulation, other than the model derivation, none of our results were analytical: our attention was mostly focused on a numerical investigation of the new model. However, an analytical investigation of this model could be fruitful. Our numerical results give rise to several questions that could be investigated analytically, e.g.: can we give a quantitative answer as to why the deviation between uniform and nonuniform field problems behaves as it does; can we give analytical bounds to ensure that the uniform field is always a good approximation under conditions of interest; or can we predict the asymptote observed at large $\mathcal{F}$ (with Υ fixed) seen in Figure 4.5.

It would also be of interest to include the time-dependence in the non-uniform field model. The steady state model gives a useful guide to the importance of non-uniform field effects; but time-dependence is undoubtedly important in any real device, where the switching field is applied only for a short duration. A time-dependent model is needed in order to quantify whether non-uniform field effects may be more important in the real problem where the electric field is applied only transiently. Equally important could be the influence of 2D (or 3D) effects in the non-uniform field model – it may be the case that nonuniformities in the electric field

can be larger outside the confines of the simple 1D model. Moreover, a 2D model is the minimum that might tell us about the importance of neglected end effects in our model, near the ends of the electrodes.

Finally, though we considered a 2D model for the director, at no stage did we discuss 3D effects. This means that we have neglected "twist" distortions, which may be important (useful) in a real device.

REFERENCES

[1] Press, W.H., Teukolsky, S.A., Vetterling, W.T., Flannery, B.P. (1996) *Numerical Recipes in Fortran 90* (2nd Edition). Cambridge University Press, Cambridge, UK.

[2] Blinov, L.M., Kolovsky, M., Nagata, T., Ozaki, M., Yoshino, K. (1999) Influence of guest conformation (rod- or banana-like photo-isomers) on flexoelectric coefficients in nematic liquid crystals. *Jpn. J. Appl. Phys.* **38**, L1042-L1045.

[3] Bryan-Brown, G.P., Brown, C.V., Jones, J.C. (1995) *Zenithal Bistable Device*. U.S. Patent 6249332.

[4] Chandrasekhar, S. (1992) *Liquid Crystals* (2nd Edition). Cambridge University Press, Cambridge, UK.

[5] Chen, T.-J., Chu, K.-L. (2008) Pretilt angle control for single-cell-gap transflective liquid crystal cells. *Appl. Phys. Lett.* **92** (9), 091102.

[6] Choi, M.-C., Kim, Y., Ha, C.-S. (2008) Polymers for flexible displays: from material selection to device applications. *Prog. Polymer Sci.* **33** (6), 581-630.

[7] Cui, L., Jin, W., Liu, Y., Xie, P., Zhang, R., Zhu, C., Wang, C. (1999) A combined method based on rubbing and UV-irradiation for preparing stable alignment layers with high pretilt angles. *Mol. Cryst. Liq. Cryst.* **333**, 135-144.

[8] Cummings, L.J., Richardson, G. (2006) Bistable nematic liquid crystal device with flexoelectric switching. *Europ. J. Appl. Math.* **17**, 435-463.

[9] Cummings, L.J., Cai, C., Kondic, L. (2013) Towards an optimal model for a bistable liquid crystal display device. *J. Eng. Math.* **80** (1), 21-38.

[10] Cummings, L.J., Cai, C., Kondic, L. (2013) Bifurcation properties of nematic liquid crystals exposed to an electric field: switchability, bistability and multistability. *Phys. Rev. E* (Submitted).

[11] Davidson, A.J., Mottram, N.J. (2002) Flexoelectric switching in a bistable nematic device. *Phys. Rev. E* **65**, 051710.

[12] DeGennes, P.G., Prost, J. (1993) *The Physics of Liquid Crystals* (2nd Edition). Oxford Science Publications, Oxford, UK.

[13] Dozov, I., Martinot-Lagarde, Ph. (n.d.) New bistable nematic LCDs using a weak anchoring boundary. *http://www.nemoptic.com/binem/publications.htm*.

[14] Hwang, J.-Y., Lee, S.H., Paek, S.K., Deo, D.-S. (2003) Tilt angle generation for nematic liquid crystal on blended homeotropic polyimide layer containing trifluoromethyl moieties. *Jpn. J. Appl. Phys.* **42** (1), 1713-1714.

[15] Kedney, P.J., Leslie, F.M. (1998) Switching in a simple bistable nematic cell. *Liquid Crystals* **24** (4), 613-618.

[16] Kim, K.-H., Baek, J.-I., Cheong, B.-H., Choi, H.-Y., Shin, S.T., Kim, J.C., Yoon, T.-H. (2010) Pretilt angle control and multidomain alignment of liquid crystals by using polyimide mixed with liquid crystalline prepolymer. *Appl. Phys. Lett.* **96** (21), 213507.

[17] Komitov, L., Barbero, G., Dahl, I., Helgee, B., Olsson, N. (2009) Controllable alignment of nematics by nanostructured polymeric layers. *Liquid Crystals* **36** (6), 747-753.

[18] Kosc, T.Z. (2005) Particle display technologies become e-paper. *Optics & Photonics News* **16** (2), 18-23.

[19] Lee, H.-J., Kang, D., Clark, C.M., Rosenblatt, C. (2009) Full control of nematic pretilt angle using spatially homogenous mixtures of two polyimide alignment materials. *J. Appl. Phys.* **105** (2), 023508.

[20] Leslie, F.M. (1979) Theory of flow phenomena in liquid crystals. *Adv. Liquid Crystals* **4**, 1-81.

[21] Lin, C.-J., Hong, G.-T., Pan, R.-P. (2009) Alignment control of rubbed polyimide layers by UV-irradiation. *Mol. Cryst. Liq. Cryst.* **512**, 911937-911945.

[22] Murthy, P.R.M., Raghunathan, V.A., Madhusudana, N.V. (1993) Experimental determination of the flexoelectric coefficients of some nematic liquid crystals. *Liquid Crystals* **14**, 483-496.

[23] Rapini, A. & Papoular, M. (1969) Distorsion d'une lamelle nématique sous champ magnétique. Conditions d'ancrage aux parois. *J. Phys. (Paris) Colloq.* **30**, C4, 54-56.

[24] Reznikov, Y., Petschek, R.G., Rosenblatt, C. (1996) Magnetic field-mediated alignment of a nematic liquid crystal at a polymer surface exposed to ultraviolet light. *Appl. Phys. Lett.* **68** (16), 2201-2203.

[25] Seo, D.-S. (1999) Generation of high pretilt angle and surface anchoring strength in nematic liquid crystal on a rubbed polymer surface. *J. Appl. Phys.* **86** (7), 3594-3597.

[26] Seo, D.-S. (2000) Anchoring strength and high pretilt angle in nematic liquid crystal on rubbed organic solvent polyimide surfaces with trifluoromethyl moieties. *J. Korean Phys. Soc.* **36** (1), 29-33.

[27] Stewart, I.W. (2004) *The Static and Dynamic Continuum Theory of Liquid Crystals.* Taylor & Francis, London, UK.

[28] Vaughn, K.E., Sousa, M., Kang, D., Rosenblatt, C. (2007) Continuous control of liquid crystal pretilt angle from homeotropic to planar. *Appl. Phys. Lett.* **90** (19), 194102.

[29] Willman, E., Fernandez, F.A., James, R., Day, S.E. (2008) Switching dynamics of a post aligned bistable nematic liquid crystal device. *J. Disp. Technol.* **4** (3), 276-281.

[30] Wu, W.-Y., Wang, C.-C., Fuh, A.Y.-G. (2008) Controlling pre-tilt angles of liquid crystal using mixed polyimide alignment layer. *Optics Express* **16** (21), 17131-17137.

[31] Yeh, P., Gu, C. (2010) *Optics of Liquid Crystal Displays.* Wiley, Hoboken, New Jersey, USA.

[32] Yeung, F.S.-Y., Xie, F.-C., Wan, J.T.-K., Lee, F.K., Tsui, O.C.K., Sheng, P., Kwok, H.-S. (2006) Liquid crystal pretilt angle control using nanotextured surfaces. *J. Appl. Phys.* **99** (12), 124506.